

# Transferring climate change knowledge

Francesco Immorlano<sup>1,2</sup>, Veronika Eyring<sup>3,4</sup>, Thomas le Monnier de Gouville<sup>5,6</sup>, Gabriele Accarino<sup>1</sup>, Donatello Elia<sup>1</sup>, Giovanni Aloisio<sup>1,2</sup>, Pierre Gentine<sup>5\*</sup>

<sup>1</sup> Euro-Mediterranean Center on Climate Change (CMCC) Foundation, Lecce, Italy

<sup>2</sup> Department of Engineering for Innovation, University of Salento, Lecce, Italy

<sup>3</sup> Deutsches Zentrum für Luft- und Raumfahrt e.V. (DLR), Institut für Physik der Atmosphäre, Oberpfaffenhofen, Germany

<sup>4</sup> University of Bremen, Institute of Environmental Physics (IUP), Bremen, Germany

<sup>5</sup> Columbia University, New York, NY USA

<sup>6</sup> Ecole Polytechnique, Palaiseau, France

\* Correspondence to: Pierre Gentine (pg2328@columbia.edu)

**Accurate and precise climate projections are required for climate adaptation and mitigation, but Earth system models still exhibit great uncertainties. Several approaches have been developed to reduce the spread of climate projections and feedbacks, yet those methods cannot capture the non-linear complexity inherent in the climate system. Using a Transfer Learning approach, we show that Machine Learning can be used to optimally leverage and merge the knowledge gained from Earth system models simulations and historical observations to more accurately project global surface air temperature fields in the 21<sup>st</sup> century. We reach an uncertainty reduction of more than 50% with respect to state-of-the-art approaches. We give evidence that our novel method provides narrower projection uncertainty together with more accurate mean climate projections, urgently required for climate adaptation.**

## Introduction

Climate change is affecting all aspects of the Earth system, impacting ecosystems' health, placing new strains on infrastructures and affecting human migration (1, 2). Earth system models are the main tools used for assessing our changing climate, although they still exhibit substantial uncertainties in their projections, even for prescribed greenhouse gas concentrations. These uncertainties have not been reduced with the evolution of Earth system models and even increased in the latest generation participating in the Coupled Model Intercomparison Project Phase 6 (CMIP6) (3–5). These models are used to project global mean temperature rise according to several shared socioeconomic pathways (SSPs), representing future socioeconomic development scenarios linked to societal actions, such as climate change mitigation, adaptation or impacts (6). For instance, the transient climate response — i.e., the surface temperature warming at the time of carbon dioxide (CO<sub>2</sub>) doubling in response to a yearly 1% increase in per-year CO<sub>2</sub> concentration — produced by CMIP6 simulations is larger than the one produced by the model ensembles of Coupled Model Intercomparison Project Phase 3 and 5 (7). In CMIP6, the equilibrium climate sensitivity, i.e., the global temperature increase at equilibrium for a doubling of CO<sub>2</sub>, was the largest of any generation of models from the 1990s, ranging from 1.8°C to 5.6°C (7). This large uncertainty range is a significant roadblock for policymakers and climate change adaptation strategies. It is well known that most of those uncertainties in climate projections can be attributed to small-scale and “fast” physical

processes, such as clouds, convection, or ocean turbulence (5, 8–10). Better constraining these physical processes, observable on a day-to-day basis, would reduce their associated uncertainties.

In this study, we show that Transfer Learning (TL), a recent branch of Machine Learning, can more accurately project global temperature maps in the 21<sup>st</sup> century. Using TL, the knowledge gained by a pre-trained model on a data-rich task can be used as a starting point to boost the performance on a new but related task in the same domain with limited data (11). We show that, using this approach, multi-model climate projections uncertainty can be reduced by optimally fusing (uncertain) model projections and historical observations. This helps enhance the representation of future projections and their associated spatial patterns which are critical to climate sensitivity (12–14).

## Constraining climate projections

To reduce climate model projection uncertainties, various approaches have been proposed to leverage current or past climate observations to refine climate sensitivity estimates (15, 16). One group of approaches has been exploiting paleoclimate proxies (i.e., surrogates for climate variables, such as temperature), especially chemical tracers that are now routinely simulated in Earth system models, to reduce and better constrain the range of climate sensitivity (17). Paleoclimate records offer tremendous potential, but paleoclimate proxies are not exempt from potential issues since they are only surrogates of the actual variable of interest, and sometimes strong assumptions might be required to link those proxies to climate variables.

A second group of approaches has used more recent climate observations, such as from the 20<sup>th</sup> century — which do not require proxies but cover a shorter time period — to constrain the range of climate sensitivity. One such prominent approach has been the use of emergent constraints. They relate a physical process, which is an important regulator of climate sensitivity (e.g., low cloud reflectivity), and its spread across models to an observation that is used to constrain future climate sensitivity within a Bayesian framework (10, 18–21). These methods, however, also suffer from several issues as they assume a linear relationship between the constraining and the target variable. In contrast, many important climate feedbacks are nonlinear (21–24), and emergent constraints are typically cast in terms of a univariate constraint, whereas many processes can interact and be multivariate. Moreover, emergent constraints are critically dependent on the model ensemble used (25) and do not account for the pattern effect, which refers to the dependence of the Earth’s outgoing radiation on the global surface warming pattern and results important for climate sensitivity (26).

Simple toy zero-order models of the Earth’s climate can also be used to understand the response of the global climate (27, 28), and especially the role of the different climate feedbacks such as those from water vapor or clouds. Recently, reduced complexity models were developed to this aim, resulting in less computationally demanding and describing the global climate at the annual scale in terms of macro-properties of the climate system (29, 30). Yet, the spatial patterns of climate response and sea surface temperature or the subtle response of cloud-circulation feedback are important for the overall climate sensitivity response. These subtleties cannot directly be resolved if toy climate models are used (27, 31). Even though Earth system

models still exhibit biases (e.g., in low cloud cover), they simulate many of the key inherent feedbacks and their spatial variability that play an important role in the climate system.

More accurate projections can be achieved using optimal corrections based on historical observations. Indeed, available observed warming trends over the last decades have been used in several studies to constrain model-based temperature projections over the 21st century directly. Tokarska et al., 2020 (32) reduced the uncertainty in future projections by downweighing those CMIP6 models whose simulation results do not agree with historical warming. Ribes et al., 2021 (33) constrained global mean temperature projections using a linear inverse method (kriging) combining CMIP6 simulations and historical warming observations since 1850. Liang et al., 2020 (34) exploited a weighting method that takes both model quality and independence into account (35) to give more weight to CMIP6 models that better match the observed 1970–2014 warming. It is worth noting that these constraints do not consider the “pattern effect” in their temperature projections as they are computed against global average temperatures (36).

Finally, the Intergovernmental Panel on Climate Change Working Group I (IPCC WGI) assessed global surface air temperature change in the Sixth Assessment Report (AR6) using multiple lines of evidence including CMIP6 projections up to 2100. CMIP6 projections were combined with observational constraints on simulated past warming to update estimates in the AR6 (37).

Recently, TL has proven to be a powerful tool in scientific applications such as weather/climate prediction (38), and environmental remote sensing (39). Moreover, TL techniques have been successfully applied to merge the knowledge of climate model simulations and observations to make long-lead El-Niño Southern Oscillation forecasts (40, 41). With respect to these approaches, this work represents, to our knowledge, the first application of Machine Learning and especially TL to reduce the spread of global climate temperature projection as well as to improve the accuracy of climate projections and their spatial patterns.

## **Leave-one-out cross-validation approach**

In the proposed approach, the near-surface air temperature fields simulated by 22 CMIP6 models (Table S1) are gathered for SSPs 2-4.5, 3-7.0, and 5-8.5. The temporal range covers 1850–2098 time period, since 2098 is the last projection year available in all the selected CMIP6 models’ simulations. For each scenario, 22 Deep Neural Networks (DNNs), one for each CMIP6 model, emulate the spatial fields of annual surface air temperature in response to greenhouse gases and aerosol forcing (see Materials and Methods and Fig. S1A). The DNNs share the same architecture and hyperparameters. They are trained to map the annual CO<sub>2</sub> equivalent scalar value to the corresponding annual surface air temperature field over the 1850–2098 time period. The year 2095 is excluded from the training set and reserved for validation purposes (see Materials and Methods). Training on the 1850–2098 period allows the DNNs to learn both historical and future temperature patterns. This approach results in a total of 66 (22 CMIP6 models × 3 SSP scenarios) DNNs trained to emulate CMIP6 temperature projections. We propose a TL approach to reduce the multi-model projections uncertainty by fusing climate model projections with the knowledge from historical observative data. To prove the effectiveness of our approach, the CMIP6 simulations are first used as “synthetic” observations

in a leave-one-out cross-validation framework (42). Specifically, for each SPP scenario, one CMIP6 model is removed from the ensemble and its simulation data are used as ground truth (i.e., as “synthetic historical observations”). The remaining 21 pre-trained DNNs for the considered scenario are then adjusted using a TL procedure which consists in fine-tuning each DNN by further training its neuron weights on the synthetic observations data from 1850 to 2022 (Fig. S1B-1). We then use the 21 fine-tuned DNNs to project the global surface air temperature maps from 2023 to 2098 (Fig. S1B-2). The aforementioned leave-one-out procedure is repeated for all the 22 CMIP6 models and all three SSPs. The global average temperature error, Root Mean Square Error (RMSE), percentage of uncertainty reduction, accuracy, and 5% and 95% in 2081–2098 are computed for the three SSP scenarios considered (see Materials and Methods and Table S2).

In the following, we use SSP2-4.5 as a reference since low-emission scenarios are currently more likely by the end of the century than the high-emission SSP5-8.5 (43). Our approach shows a mean global average error of  $0.34^{\circ}\text{C}$  and a mean global average RMSE of  $0.36^{\circ}\text{C}$ , in the 2081–2098 time period, with respect to the synthetic CMIP6 observations across all the 22 taken-out models under SSP2-4.5 (Table S2) The description of each metric is reported in the Supplementary Material (section Metrics). As an example, Fig. 1A shows the narrow 5–95% confidence range ( $2.79$ – $3.57^{\circ}\text{C}$ ) of the global average temperature projections for 2098 relative to the 1850–1900 base period, when FGOALS-f3-L is used as synthetic observation. This reveals that the proposed approach is effective at narrowing the temperature uncertainty range (i.e., increasing the precision). Moreover, the global average error between the average temperatures projected by the DNNs ensemble (bold green line in Fig. 1A) and the “synthetic” observations from FGOALS-f3-L (bold orange line in Fig. 1A) is equal to 0.17 in the 2081–2098 time period (Table S2). This confirms that a good accuracy is also achieved. The role of TL is to transfer prior information coming from the CMIP6 models and combine it with the retraining on the historical (1850–2022) taken-out model simulation, therefore being able to accurately extrapolate beyond historical observations. In addition, we are able to spatially project all the complexity of surface air temperature consistently replicating the details of future spatial features — such as the land-ocean contrast, the Arctic Amplification, the gradient of warming between Tropics and mid-latitudes, or colder temperatures over Greenland (Fig. 1B–D).

## Transfer Learning on Observational Data

The leave-one-out cross-validation procedure demonstrates the effectiveness of transferring knowledge from the climate models to “synthetic” observations, allowing extrapolation beyond the historical regime. The same strategy is then applied to the observed global surface air temperature maps gathered from the Berkeley Earth Surface Temperatures (BEST) dataset, including observational noise (see Materials and Methods). Observational data are used for transferring knowledge and constraining CMIP6 models simulations on a common historical period to reduce the models’ uncertainty on future projections. In particular, the DNNs pre-trained on CMIP6 simulation data over 1850–2098 are “transfer learned” on the BEST data covering the 1979–2022 time period, still using annual  $\text{CO}_2$  equivalent as predictor (Fig. S1C–

1). The resulting fine-tuned DNNs are then used to project global surface air temperature maps over the 2023–2098 period, for each SSP scenario (Fig. S1C-2). In the following, the SSP2-4.5 scenario is used again as reference, and predicted future warming values are computed with respect to the 1850–1900 baseline period. The ensemble mean and spread (5–95% range) across the DNNs are used to project future climate change. Our estimated global annual-mean temperature increase by 2098 is 2.69°C (2.41–3.07°C). This can be compared to the CMIP6 inter-model equal-weight mean of 2.79°C (1.65–3.92°C) (Fig. 2). The equal-weight mean CMIP6 models’ projection of global temperature is comparable to the one projected by the DNNs ensemble, building further confidence in our approach. Concerning the 2081–2098 time period, we observe a reduction of about 71% on the overall uncertainty range with respect to the unconstrained CMIP6 models (Fig. 3 and Table S3). It is worth noting that the spread in the CMIP6 mean global temperature projection is typically sensitive to the subset of models used for the ensemble in the standard CMIP6 projections. This is not the case in our approach, as all the DNNs trained on independent models and then fine-tuned on historical temperature data are projecting nearly the same global temperature rise after TL (Fig. 2). Further, model filiation does not impact the result, as the models exhibit the same performance whether or not they share some lineage (Supplementary Material).

In comparison to other state-of-the-art methods aimed at narrowing down the model-based projections uncertainty, we find a 48% reduction in projection uncertainty with respect to Ribes et al., 2021 (33), 55% with respect to Liang et al., 2020 (34), and 59% with respect to Tokarska et al., 2020 (32) under SSP2-4.5. Moreover, we obtained a 55% reduction with respect to the 5–95% range assessed by IPCC WGI (37) (Fig. 3 and Table S3). Even our near-term (2021–2040) (37) and mid-term (2041–2060) (37) projections result in an agreement but with a smaller spread with respect to the IPCC AR6 evaluation, corresponding to a percentage uncertainty reduction equal to 70% (near-term) and 58% (mid-term), respectively (Table S4). The aforementioned results are confirmed also for SSP3-7.0 and 5-8.5, even if the reduction in the uncertainty is smaller (Fig. 3 and Tables S3, S4).

The Paris Agreement aims to “hold the increase in the global average temperature to well below 2°C above pre-industrial levels and to pursue efforts to limit the temperature increase to 1.5°C above pre-industrial levels” (37). From the analysis made by the IPCC WGI in the AR6, the central estimate of crossing the 1.5°C threshold is found to be in the “early 2030s” (in all SSPs except 5-8.5), about 10 years earlier than the midpoint of the likely range (2030–2052) communicated in the Special Report (44) on 1.5°C in which continuation on the current warming rate was assumed (37). Moreover, surpassing the 1.5°C threshold was recently estimated by the European Center for Medium-Range Weather Forecast between 2030 and 2035, using a linear extrapolation of the current global warming trend (45). Diffenbaugh and Barnes (46) predicted that 1.5°C and 2°C will be reached in 2033 (2028–2039) and 2049 (2043–2055), respectively (Table S5). According to our results, the 1.5°C global threshold (relative to 1850–1900) will be exceeded in 2033 (2029–2036) under SSP2-4.5. Similarly, the 2°C threshold will be exceeded in 2054 (2047–2063) (Table S5). Each of those years is computed as the first year at which 21-year running averages of surface air temperature exceed the given global warming level, as done in Chapter 4 of the IPCC WGI AR6 (37). Our TL DNNs ensemble is in line with the aforementioned state-of-the-art estimates although the stronger retrieved spatial patterns, especially the Arctic Amplification that most CMIP6 models

still tend to underestimate (47). The impact of spatial variability on warming is captured by the DNNs and used to reduce historical global surface air temperature biases (e.g., cold tongue, Gulf Stream, etc.) after TL on the BEST data, thus building further confidence in our method (Fig. 4 and Supplementary Text). This shows that the DNNs, when exposed to historical observative data, can learn the non-linear dependence on radiative forcing (CO<sub>2</sub> equivalent) and correct the CMIP6 models' structural errors, such as the ones due to low clouds or convection. Moreover, the regional differences of the DNNs with respect to the observative data change at different times, proving that our approach is not a simple mean bias correction (Fig. 4B).

## Conclusions

DNNs initially trained to emulate Earth system models and then fine-tuned using TL on historical global surface air temperature maps can more accurately project climate change for prescribed greenhouse gas concentrations. Using this strategy, we substantially reduced the 5–95% range of projected global surface air temperature across shared socioeconomic pathways scenarios. In particular, concerning the 5–95% warming confidence range in 2081–2098 under SSP2-4.5, we obtained a reduction of 48% with respect to the best state-of-the-art approach (33) and 55% with respect to the IPCC WGI AR6 (37). An improvement with respect to other methods was also observed under SSPs 3-7.0 and 5-8.5. Our end of century estimate of global surface air temperature increase (relative to 1850–1900) is 2.69°C (2.41–3.07°C) for SSP2-4.5. Our estimates translate into exceeding the 1.5°C threshold (with respect to 1850–1900) of the Paris' agreement in 2033 (2029–2036) under SSP2-4.5. Under the same scenario, the 2°C threshold will be exceeded in 2054 (2047–2063). Our results are in line with recent estimates from the state-of-the-art methods (including IPCC WG1 AR6 (37)) and CMIP6 Earth systems models, but with a reduced uncertainty. In addition, one of the key features of our work is the projection of annual surface air temperature maps with a global coverage instead of simply providing globally averaged annual values. However, especially for end of century projections, there are still substantial uncertainties related to future greenhouse gas concentrations scenarios. Some of those uncertainties relate to projections of the ocean and terrestrial carbon uptake (48, 49), even though there have been recent attempts to refine those model estimates (50). Yet, reducing greenhouse gas emissions is clearly the only path forward to reaching the limits set by the Paris' agreement. Some other questions related to the results achieved in this work remain open and deserve further investigations. For instance, the inclusion of interannual variability would be essential to characterize extreme events and is left for future work. Nonetheless, Machine Learning can be used to optimally combine historical observations and climate model knowledge to better project our future and provide more accurate projections for policymakers.

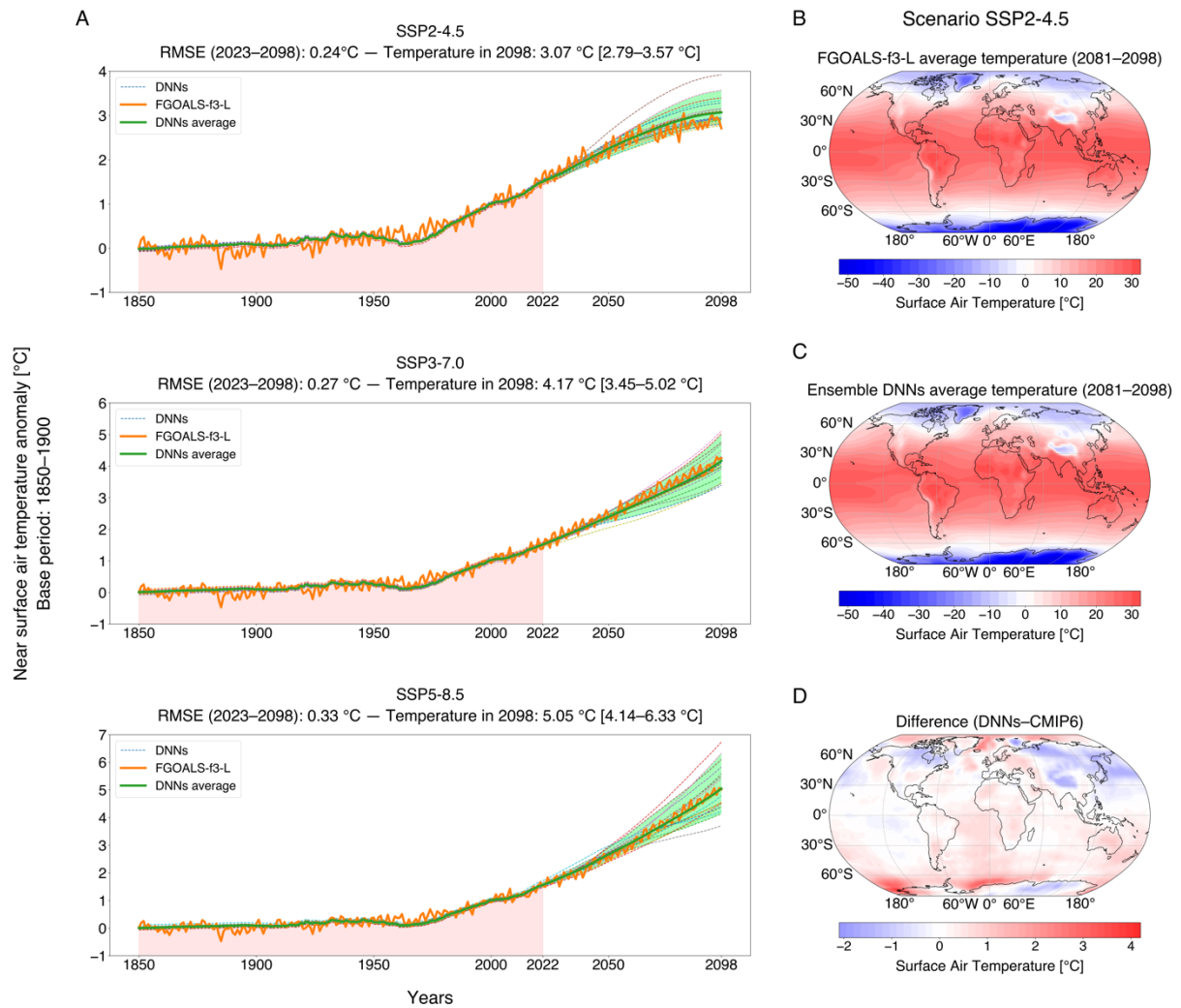


**Fig. 1. Leave-one-model-out cross-validation approach example (here for FGOALS-f3-L).** (A) Global average surface air temperature projected by the DNNs (thin dotted lines), corresponding averages across the DNNs (bold green line) for each scenario and FGOALS-f3-L simulation data (orange bold line). The projections are generated after transfer learning each DNN on the FGOALS-f3-L historical model simulations. Red shadings show the training set (1850–2022) and green shadings show the 5–95% range (numerical values for 5–95% range of temperature prediction in 2098 are reported as well). (B to D) Maps of surface air temperature projected in 2081–2098 by FGOALS-f3-L (B) and by the DNNs ensemble (average computed across maps generated by each DNN) (C) under SSP2-4.5 scenario. The difference between DNNs and CMIP6 average temperature maps is also reported (D).

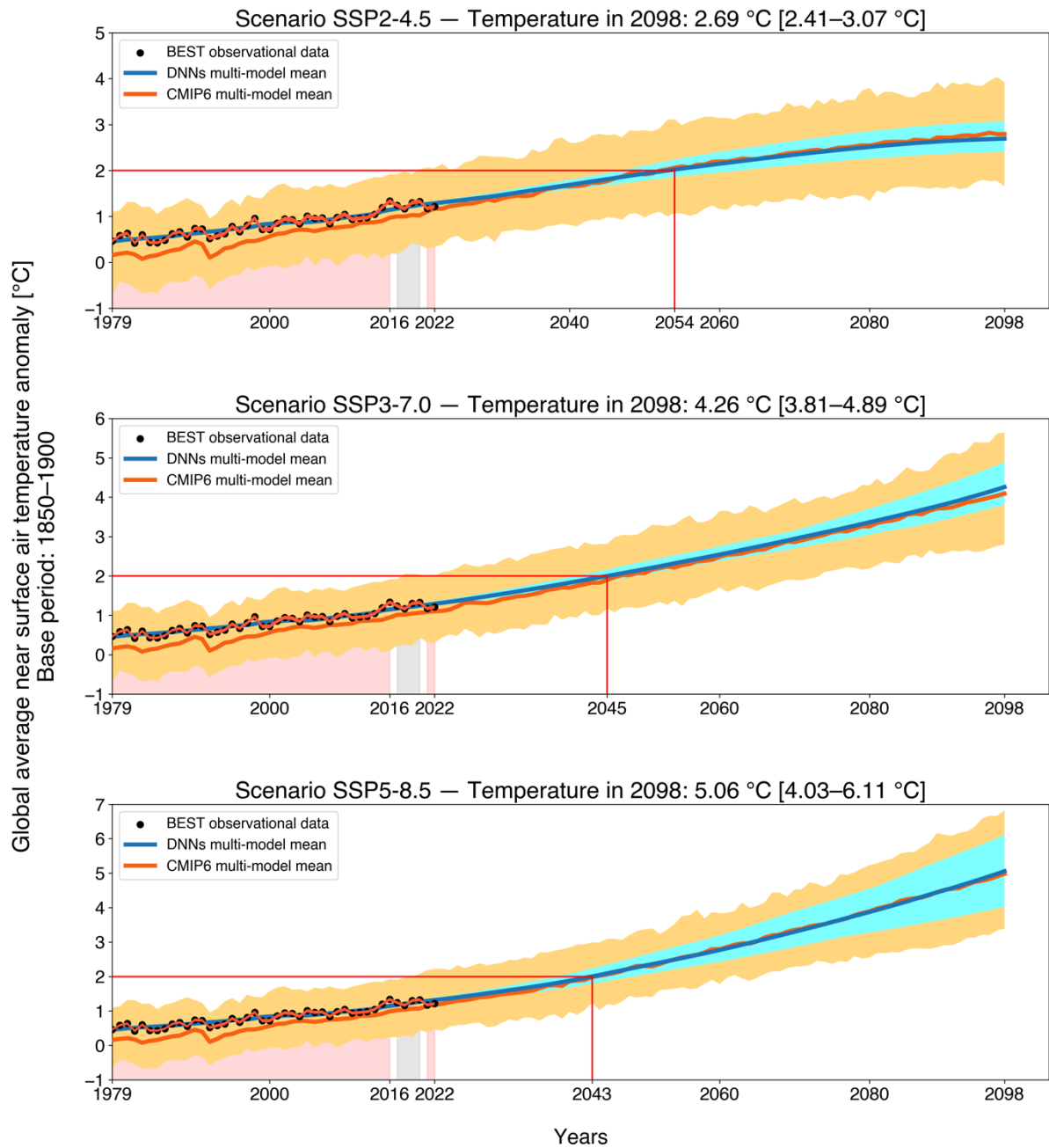


**Fig. 2. Transfer Learning on observations.** DNNs multi-model mean projections (bold blue line) of global average surface warming relative to the average over 1850–1900 for each scenario. The projections are generated after transfer learning (training set, red shading: 1979–2016, 2021, 2022; validation set, grey shading: 2017–2020) each DNN on BEST historical observational data (black dots). The red line in each plot represents the year the 2°C Paris’ Agreement threshold will be reached according to the DNNs projections. The 5–95% ranges of DNNs (light blue shading) and CMIP6 unconstrained (orange shading) projections are reported. The unconstrained CMIP6 multi-model mean (bold orange line) is shown as well. For each plot, numerical values of 5–95% range for temperature prediction in 2098 are present in square brackets.

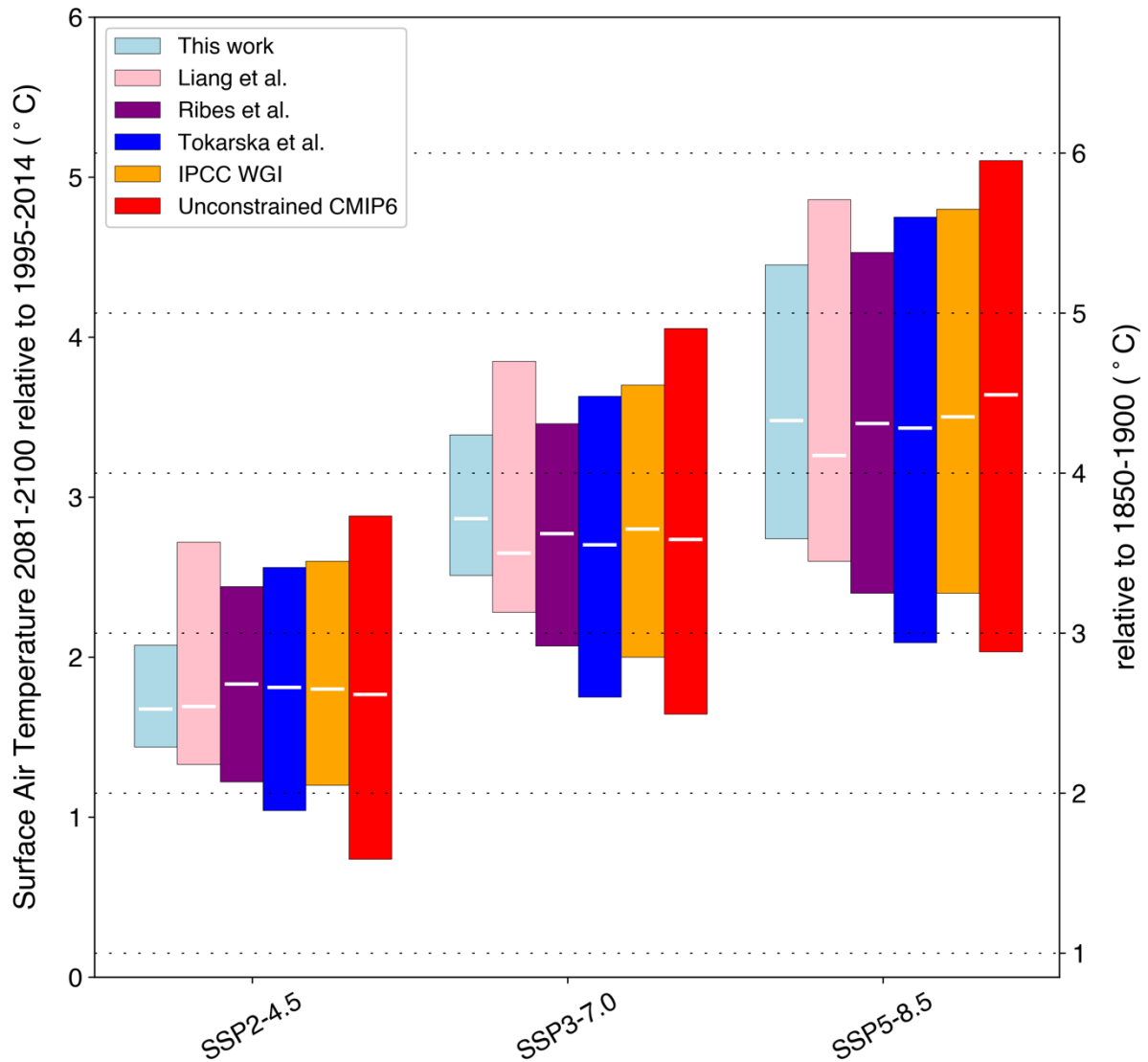


**Fig. 3. Global surface air temperature changes for the long-term period (2081–2100).** Global 5–95% warming ranges for the long-term period (2081–2100) relative to the average over 1995–2014 (left y axis) and 1850–1900 (right y axis) for SSP2-4.5, 3-7.0 and 5-8.5 scenarios. White lines for each box plot represent the temporally averaged median values. Note that the bar plots for Ribes et al. and this work are computed in the 2081–2098 time period. The remaining ones are computed in the 2081–2100 time period. These results extend those reported in Chapter 4 of the IPCC AR6 (46).

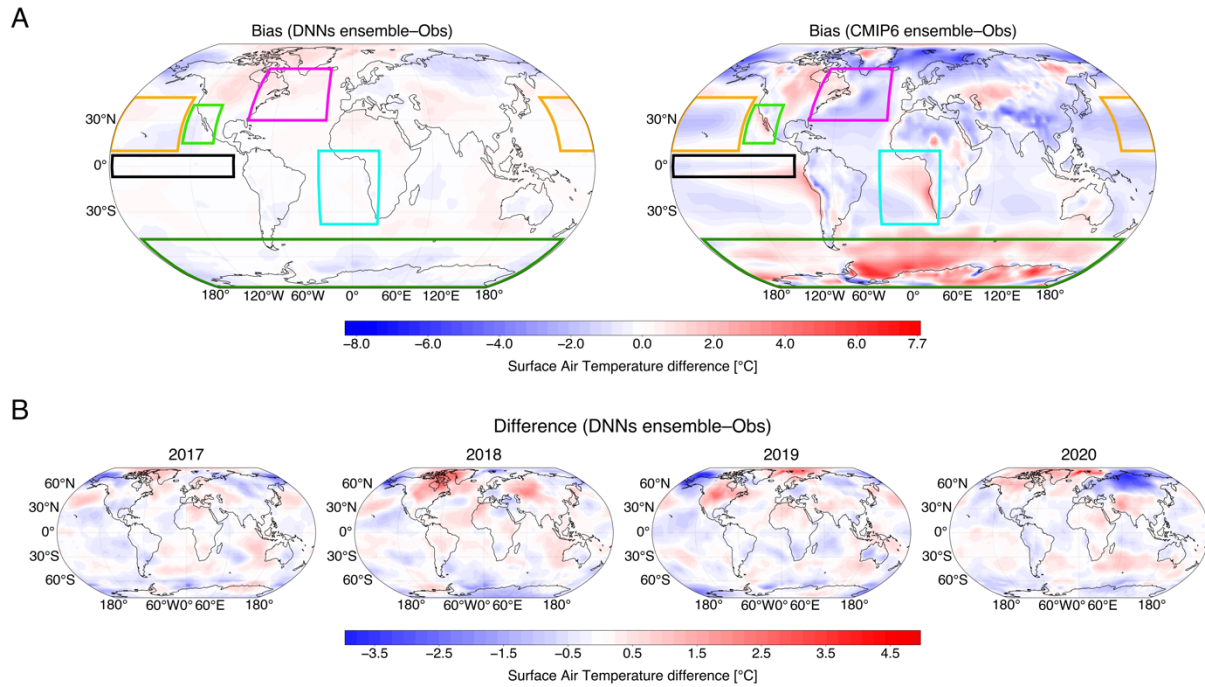


**Fig. 4. Historical bias surface air temperature maps.** Average bias surface air temperature maps in validation years (2017–2020) for SSP2-4.5. The biases of DNNs and CMIP6 ensembles with respect to the observations is reported (A). Some well-known biases are selected and highlighted with the colored boxes — Antarctic (green), cold tongue (black), Gulf Stream (purple), South East Atlantic (light blue), North West Pacific (orange), North East Pacific (light green). The bias maps are computed by averaging in time the temperature maps generated by the CMIP6 ensemble and the DNNs ensemble and subtracting them the observation maps averaged over the same years. The surface air temperature maps of the DNNs ensemble difference with respect to the observation data in each single year is also reported (B). These differences include climate variability.

## References

1. Intergovernmental Panel on Climate Change. *Climate Change 2013: The Physical Science Basis. Contribution of Working Group I to the Fifth Assessment Report of the Intergovernmental Panel on Climate Change* [Stocker, T.F., D. Qin, G.-K. Plattner, M. Tignor, S.K. Allen, J. Boschung, A. Nauels, Y. Xia, V. Bex and P.M. Midgley (eds.)]. Cambridge University Press, Cambridge, United Kingdom and New York, NY, USA, 1535 pp.
2. Intergovernmental Panel on Climate Change. *Climate Change 2014: Impacts, Adaptation, and Vulnerability. Part A: Global and Sectoral Aspects. Contribution of Working Group II to the Fifth Assessment Report of the Intergovernmental Panel on Climate Change* [Field, C.B., V.R. Barros, D.J. Dokken, K.J. Mach, M.D. Mastrandrea, T.E. Bilir, M. Chatterjee, K.L. Ebi, Y.O. Estrada, R.C. Genova, B. Girma, E.S. Kissel, A.N. Levy, S. MacCracken, P.R. Mastrandrea, and L.L. White (eds.)]. Cambridge University Press, Cambridge, United Kingdom and New York, NY, USA, 1132 pp.
3. V. Eyring, S. Bony, G. A. Meehl, C. A. Senior, B. Stevens, R. J. Stouffer, K. E. Taylor, Overview of the Coupled Model Intercomparison Project Phase 6 (CMIP6) experimental design and organization. *Geosci. Model Dev.* **9**, 1937–1958 (2016).
4. C. Tebaldi, K. Debeire, V. Eyring, E. Fischer, J. Fyfe, P. Friedlingstein, R. Knutti, J. Lowe, B. O'Neill, B. Sanderson, D. van Vuuren, K. Riahi, M. Meinshausen, Z. Nicholls, K. B. Tokarska, G. Hurtt, E. Kriegler, J. F. Lamarque, G. Meehl, R. Moss, S. E. Bauer, O. Boucher, V. Brovkin, Y. H. Byun, M. Dix, S. Gualdi, H. Guo, J. G. John, S. Kharin, Y. Kim, T. Koshiro, L. Ma, D. Olivié, S. Panickal, F. Qiao, X. Rong, N. Rosenbloom, M. Schupfner, R. Séférian, A. Sellar, T. Semmler, X. Shi, Z. Song, C. Steger, R. Stouffer, N. Swart, K. Tachiiri, Q. Tang, H. Tatebe, A. Voldoire, E. Volodin, K. Wyser, X. Xin, S. Yang, Y. Yu, T. Ziehn, Climate model projections from the Scenario Model Intercomparison Project (ScenarioMIP) of CMIP6. *Earth Syst. Dyn.* **12**, 253–293 (2021).
5. M. D. Zelinka, T. A. Myers, D. T. McCoy, S. Po-Chedley, P. M. Caldwell, P. Ceppi, S. A. Klein, K. E. Taylor, Causes of higher climate sensitivity in CMIP6 models. *Geophys. Res. Lett.* **47**, e2019GL085782 (2020).
6. B. C. O'Neill, C. Tebaldi, D. P. van Vuuren, V. Eyring, P. Friedlingstein, G. Hurtt, R. Knutti, E. Kriegler, J.-F. Lamarque, J. Lowe, G. A. Meehl, R. Moss, K. Riahi, B. M. Sanderson, The scenario model intercomparison project (ScenarioMIP) for CMIP6. *Geosci. Model Dev.* **9**, 3461–3482 (2016).
7. G. A. Meehl, C. A. Senior, V. Eyring, G. Flato, J. F. Lamarque, R. J. Stouffer, K. E. Taylor, M. Schlund, Context for interpreting equilibrium climate sensitivity and transient climate response from the CMIP6 Earth system models. *Sci. Adv.* **6**, eaba1981 (2020).
8. T. Schneider, J. Teixeira, C. S. Bretherton, F. Brient, K. G. Pressel, C. Schär, A. P. Siebesma, Climate goals and computing the future of clouds. *Nat. Clim. Change* **7**, 3–5 (2017).

9. S. Bony, B. Stevens, D. M. W. Frierson, C. Jakob, M. Kageyama, R. Pincus, T. G. Shepherd, S. C. Sherwood, A. P. Siebesma, A. H. Sobel, M. Watanabe, M. J. Webb, Clouds, circulation and climate sensitivity. *Nat. Geosci.* **8**, 261–268 (2015).
10. S. C. Sherwood, S. Bony, J.-L. Dufresne, Spread in model climate sensitivity traced to atmospheric convective mixing. *Nature* **505**, 37–42 (2014).
11. K. Weiss, T. M. Khoshgoftaar, D. Wang, A survey of transfer learning. *J. Big Data* **3**, 9 (2016).
12. B. E. J. Rose, K. C. Armour, D. S. Battisti, N. Feldl, D. D. B. Koll, The dependence of transient climate sensitivity and radiative feedbacks on the spatial pattern of ocean heat uptake. *Geophys. Res. Lett.* **41**, 1071–1078 (2014).
13. T. Andrews, J. M. Gregory, D. Paynter, L. G. Silvers, C. Zhou, T. Mauritsen, M. J. Webb, K. C. Armour, P. M. Forster, H. Titchner, Accounting for changing temperature patterns increases historical estimates of climate sensitivity. *Geophys. Res. Lett.* **45**, 8490–8499 (2018).
14. K. C. Armour, Energy budget constraints on climate sensitivity in light of inconstant climate feedbacks. *Nat. Clim. Change* **7**, 331–335 (2017).
15. V. Eyring, P. M. Cox, G. M. Flato, P. J. Gleckler, G. Abramowitz, P. Caldwell, W. D. Collins, B. K. Gier, A. D. Hall, F. M. Hoffman, G. C. Hurtt, A. Jahn, C. D. Jones, S. A. Klein, J. P. Krasting, L. Kwiatkowski, R. Lorenz, E. Maloney, G. A. Meehl, A. G. Pendergrass, R. Pincus, A. C. Ruane, J. L. Russell, B. M. Sanderson, B. D. Santer, S. C. Sherwood, I. R. Simpson, R. J. Stouffer, M. S. Williamson, Taking climate model evaluation to the next level. *Nat. Clim. Change* **9**, 102–110 (2019).
16. S. C. Sherwood, M. J. Webb, J. D. Annan, K. C. Armour, P. M. Forster, J. C. Hargreaves, G. Hegerl, S. A. Klein, K. D. Marvel, E. J. Rohling, M. Watanabe, T. Andrews, P. Braconnot, C. S. Bretherton, G. L. Foster, Z. Hausfather, A. S. von der Heydt, R. Knutti, T. Mauritsen, J. R. Norris, C. Proistosescu, M. Rugenstein, G. A. Schmidt, K. B. Tokarska, M. D. Zelinka, An assessment of Earth’s climate sensitivity using multiple lines of evidence. *Rev. Geophys.* **58**, e2019RG000678 (2020).
17. J. E. Tierney, C. J. Poulsen, I. P. Montañez, T. Bhattacharya, R. Feng, H. L. Ford, B. Hönlisch, G. N. Inglis, S. V. Petersen, N. Sahoo, C. R. Tabor, K. Thirumalai, J. Zhu, N. J. Burls, G. L. Foster, Y. Goddérís, B. T. Huber, L. C. Ivany, S. K. Turner, D. J. Lunt, J. C. McElwain, B. J. W. Mills, B. L. Otto-Bliesner, A. Ridgwell, Y. G. Zhang, Past climates inform our future. *Science* **370**, aay3701 (2020).
18. A. Hall, P. Cox, C. Huntingford, S. Klein, Progressing emergent constraints on future climate change. *Nat. Clim. Chang.* **9**, 269–278 (2019).
19. P. M. Caldwell, M. D. Zelinka, S. A. Klein, Evaluating emergent constraints on equilibrium climate sensitivity. *J. Clim.* **31**, 3921–3942 (2018).
20. P. M. Cox, C. Huntingford, M. S. Williamson, Emergent constraint on equilibrium climate sensitivity from global temperature variability. *Nature* **553**, 319–322 (2018).
21. M. Schlund, A. Lauer, P. Gentine, S. C. Sherwood, V. Eyring, Emergent constraints on equilibrium climate sensitivity in CMIP5: Do they hold for CMIP6? *Earth Syst. Dynam.* **11**, 1233–1258 (2020).

22. T. Friedrich, A. Timmermann, M. Tigchelaar, O. E. Timm, A. Ganopolsji, Nonlinear climate sensitivity and its implications for future greenhouse warming. *Sci. Adv.* **2**, e1501923 (2016).
23. D. Coppin, S. Bony, On the Interplay Between Convective Aggregation, Surface Temperature Gradients, and Climate Sensitivity. *J. Adv. Model. Earth Syst.* **10**, 3123–3138 (2018).
24. T. Schneider, C. M. Kaul, K. G. Pressel, Possible climate transitions from breakup of stratocumulus decks under greenhouse warming. *Nat. Geosci.* **12**, 163–167 (2019).
25. F. J. M. M. Nijse, P. M. Cox, M. S. Williamson, Emergent constraints on transient climate response (TCR) and equilibrium climate sensitivity (ECS) from historical warming in CMIP5 and CMIP6 models. *Earth Syst. Dynam.* **11**, 737–750 (2020).
26. B. Langenbrunner, The pattern effect and climate sensitivity. *Nat. Clim. Chang.* **10**, 977 (2020).
27. R. Knutti, M. A. Rugenstein, Feedbacks, climate sensitivity and the limits of linear models. *Phil. Trans. R. Soc. A* **373**, 20150146 (2015).
28. R. Knutti, M. A. A. Rugenstein, G. C. Hegerl, Beyond equilibrium climate sensitivity. *Nat. Geosci.* **10**, 727–736 (2017).
29. Z. R. J. Nicholls, M. Meinshausen, J. Lewis, R. Gieseke, D. Dommenges, K. Dorheim, C. S. Fan, J. S. Fuglestedt, T. Gasser, U. Golüke, P. Goodwin, C. Hartin, A. P. Hope, E. Kriegler, N. J. Leach, D. Marchegiani, L. A. McBride, Y. Quilcaille, J. Rogelj, R. J. Salawitch, B. H. Samset, M. Sandstad, A. N. Shiklomanov, R. B. Skeie, C. J. Smith, S. Smith, K. Tanaka, J. Tsutsui, Z. Xie, Reduced Complexity Model Intercomparison Project Phase 1: Introduction and evaluation of global-mean temperature response. *Geosci. Model Dev.* **13**, 5175–5190 (2020).
30. Z. Nicholls, M. Meinshausen, J. Lewis, M. Rojas Corradi, K. Dorheim, T. Gasser, R. Gieseke, A. P. Hope, N. J. Leach, L. A. McBride, Y. Quilcaille, J. Rogelj, R. J. Salawitch, B. H. Samset, M. Sandstad, A. Shiklomanov, R. B. Skeie, C. J. Smith, S. J. Smith, X. Su, J. Tsutsui, B. Vega-Westhoff, D. L. Woodard, Reduced Complexity Model Intercomparison Project Phase 2: Synthesizing Earth System knowledge for probabilistic climate projections. *Earth's Future* **9**, 2020–001900 (2021).
31. R. C. J. Wills, D. S. Battisti, K. C. Armour, T. Schneider, C. Deser, Pattern Recognition Methods to Separate Forced Responses from Internal Variability in Climate Model Ensembles and Observations. *J. Clim.* **33**, 8693–8719 (2020).
32. K. B. Tokarska, M. B. Stolpe, S. Sippel, E. M. Fischer, C. J. Smith, F. Lehner, R. Knutti, Past warming trend constrains future warming in CMIP6 models. *Sci. Adv.* **6**, eaaz9549 (2020).
33. A. Ribes, S. Qasmi, N. P. Gillett, Making climate projections conditional on historical observations. *Sci. Adv.* **7**, eabc0671 (2021).
34. Y. Liang, N. P. Gillett, A. H. Monahan. Climate model projections of 21st century global warming constrained using the observed warming trend. *Geophys. Res. Lett.* **47**, e2019GL086757 (2020).
35. R. Knutti, J. Sedláček, B. M. Sanderson, R. Lorenz, E. M. Fischer, V. Eyring, A climate model projection weighting scheme accounting for performance and interdependence. *Geophys. Res. Lett.* **44**, 1909–1918 (2017).

36. T. Andrews, A. Bodas-Salcedo, J. M. Gregory, Y. Dong, On the effect of historical sst patterns on radiative feedback. *J. Geophys. Res. Atmospheres* **127**, e2022JD036675 (2022).
37. J.-Y. Lee, J. Marotzke, Future Global Climate: Scenario-Based Projections and Near-Term Information. In *Climate Change 2021: The Physical Science Basis. Contribution of Working Group I to the Sixth Assessment Report of the Intergovernmental Panel on Climate Change*, V. Masson-Delmotte et al., Eds. (Cambridge University Press, 2021).
38. A. Subel, Y. Guan, A. Chattopadhyay, P. Hassanzadeh, Explaining the physics of transfer learning in data-driven turbulence modeling. *PNAS Nexus* **2**, pgad015 (2023).
39. Y. Ma, S. Chen, S. Ermon, D. B. Lobell, Transfer learning in environmental remote sensing. *Rem. Sens. Env.* **301**, 113924 (2024).
40. Y. G. Ham, J. H. Kim, J. J. Luo, Deep learning for multi-year ENSO forecasts. *Nature* **573**, 568–572 (2019).
41. H. Wang, S. Hu, X. Li. An Interpretable Deep Learning ENSO Forecasting Model. *Ocean-Land-Atmos Res.* **2**, 0012 (2023).
42. R. A. Kohavi Study of Cross-Validation and Bootstrap for Accuracy Estimation and Model Selection. *Appear. Int. Jt. Conf. Artificial Intell.* **5**, 1–7 (1995).
43. D. Huard, J. Fyke, I. Capellán-Pérez, H. D. Matthews, A.-I. Partanen, Estimating the Likelihood of GHG Concentration Scenarios From Probabilistic Integrated Assessment Model Simulations. *Earth's Future* **10**, e2022EF002715 (2022).
44. IPCC, 2018. In: *Global Warming of 1.5°C. An IPCC Special Report on the impacts of global warming of 1.5°C above pre-industrial levels and related global greenhouse gas emission pathways, in the context of strengthening the global response to the threat of climate change, sustainable development, and efforts to eradicate poverty*. Cambridge University Press, Cambridge, UK and New York, NY, USA, 3–24 (2018).
45. A. Amici, Copernicus Climate Change Service. European Centre for Medium-Range Weather Forecasts (ECMWF) — Global Temperature Trend Monitor: User Guide (2021).
46. N. S. Diffenbaugh, E. A. Barnes, Data-driven predictions of the time remaining until critical global warming thresholds are reached. *Proc. Natl. Acad. Sci.* **120**, e2207183120 (2023).
47. M. Rantanen, A. Y. Karpechko, A. Lipponen, K. Nordling, O. Hyvarinen, K. Ruosteenoja, T. Vihma, A. Laaksonen, The Arctic has warmed nearly four times faster than the globe since 1979. *Commun. Earth Environ.* **3**, 168 (2022).
48. Friedlingstein P., Cox P., Betts R., Bopp L., von Bloh W., Brovkin V., Cadule P., Doney S., Eby M., Fung I., Bala G., John J., Jones C., Joos F., Kato T., Kawamiya M., Knorr W., Lindsay K., Matthews H. D., Raddatz T., Rayner P., Reick C., Roeckner E., Schnitzler K.-G., Schnur R., Strassmann K., Weaver A. J., Yoshikawa C., Zeng N., Climate-carbon cycle feedback analysis: Results from the C4MIP model intercomparison. *J. Clim.* **19**, 3337–3353 (2006).
49. C. D. Jones, V. Arora, P. Friedlingstein, L. Bopp, V. Brovkin, J. Dunne, H. Graven, F. Hoffman, T. Ilyina, J. G. John, M. Jung, M. Kawamiya, C. Koven, J. Pongratz, T. Raddatz, J. T. Randerson, S. Zaehle, C4MIP—The Coupled Climate–Carbon Cycle

- Model Intercomparison Project: Experimental protocol for CMIP6. *Geosci. Model Dev.* **9**, 2853–2880 (2016).
50. S. Wenzel, P. M. Cox, V. Eyring, P. Friedlingstein, Projected land photosynthesis constrained by changes in the seasonal cycle of atmospheric CO<sub>2</sub>. *Nature* **538**, 499–501 (2016).
  51. K. E. Taylor, Truly Conserving with Conservative Remapping Methods. *Geosci. Model Dev.* **17**, 415–430 (2023).
  52. J. Tsutsui, Minimal CMIP Emulator (MCE v1.2): a new simplified method for probabilistic climate projections. *Geosci. Model Dev.* **15**, 951–970 (2022).
  53. M. Meinshausen, Z. R. J. Nicholls, J. Lewis, M. J. Gidden, E. Vogel, M. Freund, U. Beyerle, C. Gessner, A. Nauels, N. Bauer, J. G. Canadell, J. S. Daniel, A. John, P. B. Krummel, G. Luderer, N. Meinshausen, S. A. Montzka, P. J. Rayner, S. Reimann, S. J. Smith, M. van den Berg, G. J. M. Velders, M. K. Vollmer, R. H. J. Wang, The shared Socio-economic Pathway (SSP) greenhouse gas concentrations and their extensions to 2500. *Geosci. Model Dev.* **13**, 3571–3605 (2020).
  54. M. Etminan, G. Myhre, E. J. Highwood, K. P. Shine, Radiative forcing of carbon dioxide, methane, and nitrous oxide: A significant revision of the methane radiative forcing, *Geophys. Res. Lett.* **43**, 12,614–12,623 (2016).
  55. R. A. Rohde, Z. Hausfather, The Berkeley Earth Land/Ocean Temperature Record. *Earth Syst. Sci. Data* **12**, 3469–3479 (2020).
  56. M. Valdenegro-Toro, D. S. Mori, “A Deeper Look into Aleatoric and Epistemic Uncertainty Disentanglement”, in *2022 IEEE/CVF Conference on Computer Vision and Pattern Recognition Workshops (CVPRW)* (IEEE, 2022).
  57. J. S. Caldeira, B. A. Nord, Deeply uncertain: comparing methods of uncertainty quantification in deep learning algorithms. *Mach. Learn. Sci. Technol.* **2**, 015002 (2020).
  58. R. Rohde, Z. Hausfather, Berkeley Earth Combined Land and Ocean Temperature Field, Jan 1850–Nov 2019, version v1. Zenodo (2019).
  59. B. Lakshminarayanan, A. Pritzel, C. Blundell, “Simple and scalable predictive uncertainty estimation using deep ensembles”, in *Advances in Neural Information Processing Systems*, vol. 30 (Curran Associates, Inc., 2017).
  60. Y. Gal, Z. Ghahramani, “Dropout as a Bayesian approximation: representing model uncertainty in deep learning”, in *Proceedings of the 33rd International Conference on Machine Learning*, vol. 48 (JMLR, 2016).
  61. C. Riquelme, G. Tucker, J. Snoek, Deep Bayesian Bandits Showdown: An Empirical Comparison of Bayesian Deep Networks for Thompson Sampling. arXiv:1802.09127 [stat.ML] (2018).
  62. I. Osband, X. Wen, S. M. Asghari, B. O’Donoghue, B. Hao, D. Lawson, M. Ibrahimi, X. Lu, V. Dwaracherla, and B. Van Roy, “The neural testbed: Evaluating joint predictions”, in *Advances in Neural Information Processing Systems*, vol. 35 (Curran Associates, Inc., 2022)
  63. J. Sicking, M. Akila, M. Pintz, T. Wirtz, “A Novel Regression Loss for Non-Parametric Uncertainty Optimization”, paper presented at 3rd Symposium on Advances in Approximate Bayesian Inference, Virtual event, January–February 2021).

64. M. D. Zeiler, G. W. Taylor, R. Fergus, “Adaptive deconvolutional networks for mid and high level feature learning” in *2011 International Conference on Computer Vision* (IEEE, 2011).
65. D. P. Kingma, J. Ba, Adam : a method for stochastic optimization. arXiv:1412.6980 [cs.LG] (2014).
66. S. J. Pan, Q. Yang, A survey on transfer learning. *IEEE Trans. Knowl. Data Eng.* **22**, 1345–1359 (2010).
67. A. L. Maas, A. Y. Hannun, A. Y. Ng, Rectifier nonlinearities improve neural network acoustic models. in *Proceedings of the 30th International Conference on Machine Learning*, vol. 28 (JMLR, 2013).
68. T. Mauritsen, B. Stevens, E. Roeckner, T. Crueger, M. Esch, M. Giorgetta, H. Haak, J. Jungclaus, D. Klocke, D. Matei, U. Mikolajewicz, D. Notz, R. Pincus, H. Schmidt, L. Tomassini, Tuning the climate of a global model. *J. Adv. Model. Earth Syst.* **4**, M00A01 (2012).
69. F. Hourdin, T. Mauritsen, A. Gettelman, J.-C. Golaz, V. Balaji, Q. Duan, D. Folini, D. Ji, D. Klocke, Y. Qian, F. Rauser, C. Rio, L. Tomassini, M. Watanabe, D. Williamson, The art and science of climate model tuning. *Bull. Am. Meteorol. Soc.* **98**, 589–602 (2017).
70. M. D. Thomas, A. V. Fedorov, The Eastern Subtropical Pacific Origin of the Equatorial Cold Bias in Climate Models: A Lagrangian Perspective. *J. Clim.* **30**, 5885–5900 (2022).
71. B. Tian, X. Dong, The double-ITCZ Bias in CMIP3, CMIP5 and CMIP6 models based on annual mean precipitation. *Geophys. Res. Lett.* **47**, e2020GL087232 (2020).
72. X. Wu, Y. M. Okumura, P. N. DiNezio, S. G. Yeager, C. Deser, C. The Equatorial Pacific Cold Tongue Bias in CESM1 and Its Influence on ENSO Forecasts. *J. Clim.* **35**, 3261–3277 (2022).
73. M. Previdi, K. L. Smith, L. M. Polvani, Arctic amplification of climate change: a review of underlying mechanisms. *Environ. Res. Lett.* **16**, 093003 (2021).
74. P. J. Athanasiadis, F. Ogawa, N.-E. Omrani, N. Keenlyside, R. Schiemann, A. J. Baker, P. L. Vidale, A. Bellucci, P. Ruggieri, R. Haarsma, M. Roberts, C. Roberts, L. Novak, S. Gualdi, Mitigating Climate Biases in the Midlatitude North Atlantic by Increasing Model Resolution: SST Gradients and Their Relation to Blocking and the Jet. *J. Clim.* **35**, 6985–7006 (2022).
75. C. D., Roberts, F. Vitart, M. A. Balmaseda, Hemispheric impact of North Atlantic SSTs in subseasonal forecasts. *Geophys. Res. Lett.* **48**, e2020GL091446 (2021).
76. S. P. E. Keeley, R. T. Sutton, L. C. Shaffrey, The impact of North Atlantic sea surface temperature errors on the simulation of North Atlantic European region climate. *Q.J.R. Meteorol. Soc.* **138**, 1774–1783 (2012).
77. J. Schoonover, W. K. Dewar, N. Wienders, B. Deremble. Local Sensitivities of the Gulf Stream Separation. *J. Phys. Oceanogr.* **47**, 353–373 (2017).
78. D. Storkey, A. T. Blaker, P. Mathiot, A. Megann, Y. Aksenov, E. W. Blockley, D. Calvert, T. Graham, H. T. Hewitt, P. Hyder, T. Kuhlbrodt, J. G. L. Rae, B. Sinha, UK Global Ocean GO6 and GO7: a traceable hierarchy of model resolutions. *Geosci. Model Dev.* **11**, 3187 (2018).

79. A. Marzocchi, J. J.-M. Hirschi, N. P. Holliday, S. A. Cunningham, A. T. Blaker, A. C. Coward, The North Atlantic subpolar circulation in an eddy-resolving global ocean model. *J. Mar. Sys.* **142**, 126–143 (2015).
80. M. Watanabe, J. L. Dufresne, Y. Kosaka, T. Mauritsen, H. Tatebe, Enhanced warming constrained by past trends in equatorial Pacific sea surface temperature gradient. *Nat. Clim. Change* **11**, 33–37 (2021).
81. N. Maher, R. C. Inglin Wills, P. DiNezio, J. Klavanas, S. Milinski, S. C. Sanchez, S. Stevenson, M. F. Stuecker, X. Wu, The future of the El Niño–Southern Oscillation: using large ensembles to illuminate time-varying responses and inter-model differences. *Earth Syst. Dyn.* **14**, 413–431 (2023).
82. H.-B., Fredriksen, J. Berner, A. C. Subramanian, A. Capotondi, How does El Niño–Southern Oscillation change under global warming—A first look at CMIP6. *Geophys. Res. Lett.* **47**, e2020GL090640 (2020).
83. W. Cai, A. Santos, M. Collins, B. Dewitte, C. Karamperidou, J.-S. Kug, M. Lengaigne, M. J. McPhaden, M. F. Stuecker, A. S. Taschetto, A. Timmermann, L. Wu, S.-W. Yeh, G. Wang, B. Ng, F. Jia, Y. Yang, J. Ying, X.-T. Zheng, T. Bayr, J. R. Brown, A. Capotondi, K. M. Cobb, B. Gan, T. Geng, Y.-G. Ham, F.-F. Jin, H.-S. Jo, X. Li, X. Lin, S. McGregor, J.-H. Park, K. Stein, K. Yang, L. Zhang, W. Zhong, Changing El Niño–Southern Oscillation in a warming climate. *Nat. Rev. Earth Environ.* **2**, 628–644 (2021).
84. R. C. J. Wills, Y. Dong, C. Proistosescu, K. C. Armour, D. S. Battisti, Systematic climate model biases in the large-scale patterns of recent sea-surface temperature and sea-level pressure change. *Geophys. Res. Lett.* **49**, e2022GL100011 (2022).
85. T. Kohyama, D. L. Hartmann, D. S. Battisti, La Niña–like Mean-State Response to Global Warming and Potential Oceanic Roles. *J. Clim.* **30**, 4207–4225 (2017).
86. A. H. Sobel, C.-Y. Lee, S. G. Bowen, M. K. Tippett, Near-term tropical cyclone risk and coupled Earth system model biases. *Proc. Natl Acad. Sci. USA* **120**, e2209631120 (2023).
87. D. Bi, M. Dix, S. Marsland, S. O’Farrell, A. Sullivan, R. Bodman, R. Law, I. Harman, J. Srbinovsky, H. A. Rashid, P. Dobrohotoff, C. Mackallah, H. Yan, A. Hirst, A. Savita, F. B. Dias, M. Woodhouse, R. Fiedler, A. Heerdegen, Configuration and spin-up of ACCESS-CM2, the new generation Australian Community Climate and Earth System Simulator Coupled Model. *JSHESS* **70**, 225–251. (2020).
88. T. Semmler<sup>1</sup>, S. Danilov, P. Gierz<sup>1</sup>, H. F. Goessling, J. Hegewald, C. Hinrichs, N. Koldunov, N. Khosravi, L. Mu, T. Rackow, D. V. Sein, D. Sidorenko, Q. Wang, T. Jung, Simulations for CMIP6 With the AWI Climate Model AWI-CM-1-1. *J. Adv. Model. Earth Syst.* **12**, e2019MS002009 (2020).
89. T. Wu, R. Yu, Y. Lu, W. Jie, Y. Fang, J. Zhang, L. Zhang, X. Xin, L. Li, Z. Wang, Y. Liu, F. Zhang, F. Wu, M. Chu, J. Li, W. Li, Y. Zhang, X. Shi, W. Zhou, J. Yao, X. Liu, H. Zhao, J. Yan, M. Wei, W. Xue, A. Huang, Y. Zhang, Y. Zhang, Q. Shu, A. Hu, BCC-CSM2-HR: A high-resolution version of the Beijing climate center climate system model. *Geosci. Model Dev.* **14**, 2977–3006 (2021).

90. X.-Y. Rong, J. Li, H.-M. Chen, Y.-F. Xin, J.-Z. Su, L.-J. Hua, Z.-Q. Zhang, Introduction of CAMS-CSM model and its participation in CMIP6. *Clim. Change Res.* **15**, 540–544 (2019).
91. N. C. Swart, J. N. S. Cole, V. V. Kharin, M. Lazare, J. F. Scinocca, N. P. Gillett, J. Anstey, V. Arora, J. R. Christian, S. Hanna, Y. Jiao, W. G. Lee, F. Majaess, O. A. Saenko, C. Seiler, C. Seinen, A. Shao, M. Sigmond, L. Solheim, K. von Salzen, D. Yang, B. Winter, The Canadian Earth System Model version 5 (CanESM5.0.3). *Geosci. Model Dev.* **12**, 4823–4873 (2019).
92. A. Cherchi, P. G. Fogli, T. Lovato, D. Peano, D. Iovino, S. Gualdi, S. Masina, E. Scoccimarro, S. Materia, A. Bellucci, Global mean climate and main patterns of variability in the CMCC-CM2 coupled model. *J. Adv. Model. Earth Syst.* **11**, 185–209 (2019).
93. A. Voldoire, D. Saint-Martin, S. Sénési, B. Decharme, A. Alias, M. Chevallier, J. Colin, J. F. Guérémy, M. Michou, M. P. Moine, P. Nabat, R. Roehrig, D. Salas y Mélia, R. Sférian, S. Valcke, I. Beau, S. Belamari, S. Berthet, C. Cassou, J. Cattiaux, J. Deshayes, H. Douville, C. Ethé, L. Franchistéguy, O. Geoffroy, C. Lévy, G. Madec, Y. Meurdesoif, R. Msadek, A. Ribes, E. Sanchez-Gomez, L. Terray, R. Waldman, Evaluation of CMIP6 DECK Experiments With CNRM-CM6-1. *J. Adv. Modeling Earth Syst.* **11**, 2177–2213 (2019).
94. R. Sférian, P. Nabat, M. Michou, D. Saint-Martin, A. Voldoire, J. Colin, B. Decharme, C. Delire, S. Berthet, M. Chevallier, S. Sénési, L. Franchistéguy, J. Vial, M. Mallet, E. Joetzjer, O. Geoffroy, J.-F. Guérémy, M.-P. Moine, R. Msadek, A. Ribes, M. Rocher, R. Roehrig, D. Salas-y-Mélia, E. Sanchez, L. Terray, S. Valcke, R. Waldman, O. Aumont, L. Bopp, J. Deshayes, C. Éthé, G. Madec, Evaluation of CNRM Earth System model, CNRM-ESM2-1: Role of Earth system processes in present-day and future climate. *J. Adv. Model. Earth Syst.* **11**, 4182–4227 (2019).
95. B. He, Q. Bao, X. Wang, L. Zhou, X. Wu, Y. Liu, G. Wu, K. Chen, S. He, W. Hu, J. Li, J. Li, G. Nian, L. Wang, J. Yang, M. Zhang X. Zhang, CAS FGOALS-f3-L Model Datasets for CMIP6 Historical Atmospheric Model Intercomparison Project Simulation. *Adv. Atmos. Sci.* **36**, 771–778 (2019).
96. Y. Pu, H. Liu, R. Yan, H. Yang, K. Xia, Y. Li, L. Dong, L. Li, H. Wang, Y. Nie, M. Song, J. Xie, S. Zhao, K. Chen, B. Wang, J. Li, L. Zuo CAS FGOALS-g3 model datasets for the CMIP6 scenario model intercomparison project (ScenarioMIP). *Adv. Atmos. Sci.* **37**, 1081–1092. (2020).
97. J. P. Dunne, L. W. Horowitz, A. J. Adcroft, P. Ginoux, I. M. Held, J. G. John, J. P. Krasting, S. Malyshev, V. Naik, F. Paulot, E. Shevliakova, C. A. Stock, N. Zadeh, V. Balaji, C. Blanton, K. A. Dunne, C. Dupuis, J. Durachta, R. Dussin, P. P. G. Gauthier, S. M. Griffies, H. Guo, R. W. Hallberg, M. Harrison, J. He, W. Hurlin, C. McHugh, R. Menzel, P. C. D. Milly, S. Nikonov, D. J. Paynter, J. Ploshay, A. Radhakrishnan, K. Rand, B. G. Reichl, T. Robinson, D. M. Schwarzkopf, L. T. Sentman, S. Underwood, H. Vahlenkamp, M. Winton, A. T. Wittenberg, B. Wyman, Y. Zeng, M. Zhao, The GFDL Earth system model version 4.1 (GFDL-ESM 4.1): Overall coupled model description and simulation characteristics. *J. Adv. Model. Earth Syst.* **12**, e2019MS002015 (2020).

98. R. Krishnan, P. Swapna, A. D. Choudhury, S. Narayansetti, A. G. Prajeesh, M. Singh, A. Modi, R. Mathew, R. Vellore, J. Jyoti, T. P. Sabin, J. Sanjay, S. Ingle, The IITM Earth System Model (IITM ESM). arXiv:2101.03410 [physics.ao-ph] (2021).
99. E. M. Volodin, E. V. Mortikov, S. V. Kostykin, V. Y. Galin, V. N. Lykossov, A. S. Gritsun, N. A. Diansky, A. V. Gusev, N. G. Iakovlev, A. A. Shestakova, S. V. Emelina, Simulation of the modern climate using the INM-CM48 climate model. *Russ. J. Numer. Anal. Math. Model.* **33**, 367–374 (2018).
100. E. Volodin, A. Gritsun, Simulation of observed climate changes in 1850–2014 with climate model INM-CM5. *Earth Syst. Dyn.* **9**, 1235–1242 (2018).
101. O. Boucher, J. Servonnat, A. L. Albright, O. Aumont, Y. Balkanski, V. Bastrikov, S. Bekki, R. Bonnet, S. Bony, L. Bopp, P. Braconnot, P. Brockmann, P. Cadule, A. Caubel, F. Cheruy, F. Codron, A. Cozic, D. Cugnet, F. D’Andrea, P. Davini, C. de Lavergne, S. Denvil, J. Deshayes, M. Devilliers, A. Ducharne, J.-L. Dufresne, E. Dupont, C. Éthé, L. Fairhead, L. Falletti, S. Flavoni, M.-A. Foujols, S. Gardoll, G. Gastineau, J. Ghattas, J.-Y. Grandpeix, B. Guenet, E. Guez, Lionel, E. Guilyardi, M. Guimberteau, D. Hauglustaine, F. Hourdin, A. Idelkadi, S. Joussaume, M. Kageyama, M. Khodri, G. Krinner, N. Lebas, G. Levvasseur, C. Lévy, L. Li, F. Lott, T. Lurton, S. Luysaert, G. Madec, J.-B. Madeleine, F. Maignan, M. Marchand, O. Marti, L. Mellul, Y. Meurdesoif, J. Mignot, I. Musat, C. Ottlé, P. Peylin, Y. Planton, J. Polcher, C. Rio, N. Rochetin, C. Rousset, P. Sepulchre, A. Sima, D. Swingedouw, R. Thiéblemont, A. K. Traore, M. Vancoppenolle, J. Vial, J. Vialard, N. Viovy, N. Vuichard, Presentation and evaluation of the IPSL-CM6A-LR climate model. *J. Adv. Model. Earth Syst.* **12**, e2019MS002010 (2020).
102. J. Lee, J. Kim, M.-A. Sun, B.-H. Kim, H. Moon, H. M. Sung, J. Kim, Y.-H. Byun, Evaluation of the Korea Meteorological Administration Advanced Community Earth-System model (K-ACE). *Asia Pac. J. Atmos. Sci.* **56**, 381–395 (2020).
103. H. Tatebe, T. Ogura, T. Nitta, Y. Komuro, K. Ogochi, T. Takemura, K. Sudo, M. Sekiguchi, M. Abe, F. Saito, M. Chikira, S. Watanabe, M. Mori, N. Hirota, Y. Kawatani, T. Mochizuki, K. Yoshimura, K. Takata, R. O’ishi, D. Yamazaki, T. Suzuki, M. Kurogi, T. Kataoka, M. Watanabe, M. Kimoto, Description and basic evaluation of simulated mean state, internal variability, and climate sensitivity in MIROC6. *Geosci. Model Dev.* **12**, 2727–2765 (2019).
104. T. Mauritsen, J. Bader, T. Becker, J. Behrens, M. Bittner, R. Brokopf, V. Brovkin, M. Claussen, T. Crueger, M. Esch, I. Fast, S. Fiedler, D. Fläschner, V. Gayler, M. Giorgetta, D. S. Goll, H. Haak, S. Hagemann, C. Hedemann, C. Hohenegger, T. Ilyina, T. Jahns, D. Jimenéz-de-la-Cuesta, J. Jungclaus, T. Kleinen, S. Kloster, D. Kracher, S. Kinne, D. Kleberg, G. Lasslop, L. Kornbluh, J. Marotzke, D. Matei, K. Meraner, U. Mikolajewicz, K. Modali, B. Möbis, W. A. Müller, J. E. M. S. Nabel, C. C. W. Nam, D. Notz, S.-S. Nyawira, H. Paulsen, K. Peters, R. Pincus, H. Pohlmann, J. Pongratz, M. Popp, T. J. Raddatz, S. Rast, R. Redler, C. H. Reick, T. Rohrschneider, V. Schemann, H. Schmidt, R. Schnur, U. Schulzweida, K. D. Six, L. Stein, I. Stemmler, B. Stevens, J.-S. von Storch, F. Tian, A. Voigt, P. Vrese, K.-H. Wieners, S. Wilkenskjaeld, A. Winkler, E. Roeckner Developments in the MPI-M earth system

- model version 12 (MPI-ESM12) and its response to increasing CO<sub>2</sub>. *J. Adv. Model Earth Syst.* **11**, 998–1038. (2019).
105. S. Yukimoto, H. Kawai, T. Koshiro, N. Oshima, K. Yoshida, S. Urakawa, H. Tsujino, M. Deushi, T. Tanaka, M. Hosaka, S. Yabu, H. Yoshimura, E. Shindo, R. Mizuta, A. Obata, Y. Adachi, M. Ishii, The Meteorological Research Institute Earth System Model version 2.0, MRI-ESM2.0: Description and basic evaluation of the physical component. *J. Meteorol. Soc. Jpn. Ser. II* **97**, 931–965 (2019).
106. Ø. Seland, M. Bentsen, D. Olivie, T. Toniazzo, A. Gjermundsen, L. S. Graff, J. B. Debernard, A. K. Gupta, Y.-C. He, A. Kirkevåg, J. Schwinger, J. Tjiputra, K. S. Aas, I. Bethke, Y. Fan, J. Griesfeller, A. Grini, C. Guo, M. Ilicak, I. H. H. Karset, O. Landgren, J. Liakka, K. O. Moseid, A. Nummelin, C. Spensberger, H. Tang, Z. Zhang, C. Heinze, T. Iversen, M. Schulz, Overview of the Norwegian Earth System Model (NorESM2) and key climate response of CMIP6 DECK, historical, and scenario simulations. *Geosci. Model Dev.* **13**, 6165–6200 (2020).
107. Y.-C. Wang, H.-H. Hsu, C.-A. Chen, W.-L. Tseng, P.-C. Hsu, C.-W. Lin, Y.-L. Chen, L.-C. Jiang, Y.-C. Lee, H.-C. Liang, W.-M. Chang, W.-L. Lee, C.-J. Shiu, Performance of the Taiwan Earth System Model in Simulating Climate Variability Compared With Observations and CMIP6 Model Simulations. *J. Adv. Model. Earth Syst.* **13**, e2020MS002353 (2021).
108. A. A. Sellar, C. G. Jones, J. P. Mulcahy, Y. Tang, A. Yool, A. Wiltshire, F. M. O'Connor, M. Stringer, R. Hill, J. Palmieri, S. Woodward, L. de Mora, T. Kuhlbrodt, S. T. Rumbold, D. I. Kelley, R. Ellis, C. E. Johnson, J. Walton, N. L. Abraham, M. B. Andrews, T. Andrews, A. T. Archibald, S. Berthou, E. Burke, E. Blockley, K. Carslaw, M. Dalvi, J. Edwards, G. A. Folberth, N. Gedney, P. T. Griffiths, A. B. Harper, M. A. Hendry, A. J. Hewitt, B. Johnson, A. Jones, C. D. Jones, J. Keeble, S. Liddicoat, O. Morgenstern, R. J. Parker, V. Predoi, E. Robertson, A. Siahann, R. S. Smith, R. Swaminathan, M. T. Woodhouse, G. Zeng, M. Zerroukat, UKESM1: Description and evaluation of the U.K. Earth system model. *J. Adv. Model. Earth Syst.* **11**, 4513–4558 (2019).
109. R. B. Neale, A. Gettelman, S. Park, C.-C. Chen, P. H. Lauritzen, D. L. Williamson, A. J. Conley, D. Kinnison, D. Marsh, A. K. Smith, F. Vitt, R. Garcia, J.-F. Lamarque, M. Mills, S. Tilmes, H. Morrison, P. Cameron-Smith, W. D. Collins, M. J. Iacono, R. C. Easter, X. Liu, S. J. Ghan, P. J. Rasch, M. A. Taylor, “Description of the NCAR community atmosphere model (CAM 5.0)” (NCAR Tech. Note Sci. and Tech. Rep., NCAR Publication Office, Boulder, CO, 2010). [NCAR/TN-486+STR]

# Materials and Methods

## Earth System Models

We use global surface air temperature maps simulated from 1850 to 2098 by 22 Earth system models (Table S1) from the Coupled Model Intercomparison Projects Phase 6 (CMIP6) ensembles under the shared socioeconomic pathways (SSPs) 2-4.5, 3-7.0 and 5-8.5. The models are selected according to the availability of the simulations for the three SSPs. Some of the CMIP6 models' simulations are available at a spatial resolution of 250 km and others at 100 km. The conservative remapping (51) is used to align all the simulations to the CanESM5-CanOE grid which is the one at the lowest spatial resolution among them, with 64×128 grid points. The coarsest spatial resolution is selected to avoid any synthetic information that would be added in case of remapping to a higher-resolution grid. The CMIP6 simulated maps are gathered at a monthly temporal resolution, and they are averaged over a year to generate the corresponding annual version to match the temporal resolution (annual) of carbon dioxide (CO<sub>2</sub>) input data.

## CO<sub>2</sub> equivalent data

One single annual CO<sub>2</sub> equivalent value is used as forcing (predictor) to each DNN. The CO<sub>2</sub> equivalent values are computed from Effective Radiative Forcing (ERF) values that take into account aerosols and greenhouse gases such as CO<sub>2</sub>, methane, nitrous dioxide, etc. and are estimated by the Minimal CMIP Emulator v1.2 reduced-complexity model (52). We have one ERF value per year for each SSP scenario. For each ERF value we iteratively compute the corresponding CO<sub>2</sub> equivalent such that, when fed to a CO<sub>2</sub> radiative forcing formula, the output is in a distance less than 1e-5 with respect to the ERF value. The CO<sub>2</sub> radiative forcing formula used in this work is reported below. It was introduced by Meinshausen et al., 2020 (53) (for radiative forcing after stratospheric adjustments and relative to pre-industrial (1750) levels) and is an optimized modification of the simplified formula presented by Etminan et al., 2016 (54).

$$RF_{CO_2} = (\alpha' + \alpha_{N_2O}) \cdot \ln\left(\frac{C}{C_0}\right)$$

where:

$$C_{\alpha_{MAX}} = C_0 - \frac{b_1}{2a_1} \approx 1808 \text{ ppm}$$

$$\alpha' = d_1 - \frac{b_1^2}{4a_1}, \text{ for } C > C_{\alpha_{max}}$$

$$\alpha' = d_1 + a_1(C - C_0)^2 + b_1(C - C_0), \text{ for } C_0 < C < C_{\alpha_{max}}$$

$$\alpha' = d_1, \text{ for } C < C_0$$

$$\alpha_{N_2O} = c_1 \cdot \sqrt{N}$$

$$a_1 = -2.4785 \times 10^{-7} \text{ Wm}^{-2} \text{ ppm}^{-1}$$

$$b_1 = 0.00075906 \text{ Wm}^{-2} \text{ ppm}^{-1}$$

$$c_1 = -0.0021492 \text{ Wm}^{-2} \text{ ppb}^{-0.5}$$

$$d_1 = 5.2488 \text{ Wm}^{-2}$$

$$C_0 = 277.15 \text{ ppm}$$

## BEST observational data

We use historical surface air temperature estimates from the global Berkeley Earth Surface Temperatures (BEST) (55) gridded data, which are provided on a  $1^\circ \times 1^\circ$  latitude/longitude grid from 1850 to 2022 with a monthly temporal resolution. Specifically, we select the BEST maps with air temperatures at sea ice, in which temperatures in the presence of sea ice are extrapolated from land-surface air temperature. This revealed to be a more sensible approach for capturing climate change, especially at the poles. Indeed, the change of air temperatures over sea ice can be large even if the sea surface temperature under sea ice is not changing, since the latter is strictly connected to the water freezing point and can only vary with changes in sea ice cover. Over the last decades, the Arctic region was characterized by a very strong warming trend during the winter season, and this translated into an additional  $\sim 0.1^\circ\text{C}$  global-average temperature rise during the 19<sup>th</sup> century with respect to estimates not including such changes (i.e., estimates based on sea surface temperature under sea ice) (55). The conservative remapping (51) is used to align the BEST data to the same CanESM5-CanOE grid used for CMIP6 data, thus generating temperature fields of size  $64 \times 128$  and averaged over time to get one map per year. Although the temporal coverage of the BEST dataset starts from 1850, maps prior to 1979 are excluded after the remapping because of lack of data in many regions at the time and thus reduced accuracy prior to 1979. For this reason, the temporal domain used is 1979–2022.

In order to take into account aleatoric uncertainty (i.e., uncertainty related to the inherent randomness of a given phenomenon), a noise is added to each annual BEST map by sampling the noise value from a Gaussian distribution (56, 57) with 0 mean and standard deviation equal to the annual uncertainties — provided by the Berkeley Earth group and available with the dataset — representing the statistical and spatial undersampling effects as well as ocean biases (58). This allows accounting for the noise in BEST observative data. To include epistemic uncertainty (i.e., uncertainty due to lack of knowledge by the model about the phenomenon of interest), an ensemble technique (59) is exploited. Specifically, 5 datasets are built for each CMIP6 model and for each scenario by adding the random Gaussian noise to the BEST temperature maps, thus obtaining an ensemble of 330 (i.e.,  $5 \times 22 \times 3$ ) datasets of historical observations. This allows estimating structural and aleatoric uncertainties and the noise due to internal climate variability. We tried 10 and 20 BEST-perturbed datasets per model and scenario as well, but did not obtain substantial improvements. We did not evaluate Monte Carlo dropout (60) for the quantification of aleatoric uncertainty as it has been shown to underestimate uncertainty (61–63).

## Transfer Learning Approach

The first step of the algorithm involves the use of Deep Neural Networks (DNNs) to emulate and replicate the annual surface air temperature maps simulated by 22 CMIP6 models (Table S1) participating in the Scenario Model Intercomparison Project (6). These models cover the Earth’s global surface and are selected for SSPs 2-4.5, 3-7.0 and 5-8.5. To achieve this, an

individual DNN is trained for each CMIP6 model simulation (Fig. S1A). Each DNN predicts annual temperature maps starting from the annual CO<sub>2</sub> equivalent concentration, including aerosols and the radiative effect of other greenhouse gases, such as methane. These inputs are readily available in most models and the objective is to generate one surface air temperature map per year. In total, 66 DNNs are implemented and trained, representing the combination of 22 CMIP6 models and 3 SSPs. The training is performed using data from 1850 to 2098, since 2098 is the last projection year available in all the selected CMIP6 models' simulations. Moreover, the year 2095 was reserved for validation purposes.

To reduce the uncertainty of the multi-model projections, this work proposes using Transfer Learning (TL) to combine model projections with the information from historical observational data. To evaluate the potential of our TL strategy, for each scenario, one of the 22 CMIP6 simulations is taken out and used as a synthetic truth for validation in a leave-one-out cross-validation approach (42). Specifically, each DNN trained on the remaining 21 CMIP6 simulations is “transfer learned” on the left-out simulation for the corresponding scenario by updating its weights on the (simulated) historical data from 1850 to 2022 (Fig. S1B). In other words, the DNNs that were initially trained to reproduce the CMIP6 models are now fine-tuned on the historical data simulated by the left-out model. The 21 fine-tuned DNNs are then used to project the global surface air temperature maps from 2023 to 2098 to reproduce the temperatures projected by the left-out model. This procedure is then repeated for all the 22 CMIP6 models and all the three SSP scenarios.

The goal of the TL just described above and applied to simulation data is to test the capacity of the approach before applying the same method to observational data to constrain the warming projections, which is done in the next step. Indeed, as done for the leave-one-out cross-validation, one DNN per CMIP6 model is trained on the corresponding surface air temperature global maps from 1850 to 2098 for the three SSP scenarios, thus implementing and training a total of 66 DNNs (Fig. S1A). For each scenario, this results in one climate temperature projection per model. Then, using an ensemble technique (59) (to address epistemic uncertainty) and the TL strategy, the DNN model weights and biases are fine-tuned 5 times independently on the historical BEST dataset (1979–2022), each time perturbed through the addition of a noise randomly sampled from a Gaussian distribution (thus addressing aleatoric uncertainty) (Fig. S1C). The years 2017–2020 are reserved for validation.

## Deep Neural Networks

The DNNs designed and implemented for each model and scenario share the same architecture and hyperparameters configuration. Deconvolutional (or transposed convolutional) layers (64) are used to generate temperature maps from CO<sub>2</sub> equivalent scalar values. The scalar input is fed to a dense layer made up of  $4 \times 8 \times 128$  neurons. Then, four deconvolutional layers have the role of modelling the correlated spatial information and upsampling it in order to perform the deconvolutions and reach the spatial resolution of the target map. Specifically, each deconvolutional layer is characterized by 128 kernels with size  $10 \times 10$  and stride equal to 2: this allows doubling the dimension of rows and columns of the activation volume received by the layer as input. The last deconvolutional layer returns an activation volume of size  $64 \times 128 \times 128$ . A final convolutional layer with one kernel of size  $5 \times 5$  and stride equal to 1 is

needed to refine the spatial information generated by the previous deconvolutional layers and to generate the final near-surface air temperature map of size  $64 \times 128$ . The best set of hyperparameters was found after a trial-and-error procedure involving several configurations. We tested different learning rates for the first training by progressively increasing the value from  $1e-8$  to  $1e-2$ . We selected a learning rate equal to  $1e-4$  as it revealed a good trade-off between generalization accuracy and convergence time even across different hyperparameters configurations. In the end, the Adam optimizer (65), a learning rate of  $1e-4$ , a batch size of 8 and 500 epochs are used for the first training. During TL, we fine-tune the pre-trained layers selecting a lower learning rate to not dramatically change the values of the weights adjusted during the first training. This is done when training on new data with the aim of keeping the old knowledge previously acquired and transferring it to the new learning (66). We found good performance with a learning rate an order of magnitude smaller than the one used during the first training, which is a common practice in fine-tuning. The strategy of freezing some layers during TL was tested as well, but it led to worse results. The final set of hyperparameters for TL is a learning rate of  $1e-5$ , Adam optimizer (65), a batch size of 16 and 500 epochs. The DNN architecture is the same for both training and TL phases. The loss is a standard Mean Absolute Error and both the annual  $\text{CO}_2$  equivalent values, and the surface air temperature maps are scaled using Min-Max Normalization in the 0–1 range. Leaky Rectified Linear Unit activation function (67) is selected for the hidden layers and a sigmoid is used for the output layer because of the 0–1 range of Min-Max Normalization of both input and output.

## Metrics

For each iteration of the leave-one-out cross validation in which a CMIP6 model is removed (taken-out model  $i$ ) from the ensemble, the following metrics are computed, and the corresponding values are reported in Table S2:

$$DNNs \text{ ensemble per year} = DE_i^{(y)} = \frac{1}{21} \sum_{m=1}^{21} \hat{T}_{m,i}^{(y)}$$

where:

- $y \in \{2081, \dots, 2098\}$
- $m \in \{1, \dots, 21\}$  is the index of one of the 21 remaining CMIP6 models that are fine-tuned on the taken-out model  $i$
- $i \in \{1, \dots, 22\}$  is the index of one of the 22 CMIP6 models that is removed from the ensemble during the leave-one-out cross validation
- $\hat{T}_{m,i}^{(y)}$  is the global temperature value predicted by the DNN (pre-trained on the  $m_{th}$  CMIP6 model and fine-tuned on the taken-out model  $i$ ) for year  $y$

$$Global \text{ average error}_i = \frac{1}{18} \sum_{y=2081}^{2098} \left( DE_i^{(y)} - T_i^{(y)} \right)$$

where:

$T_i^{(y)}$  is the global temperature value simulated by the CMIP6 taken-out model  $i$  for the year  $y$

$$Global\ RMSE_i = \sqrt{\frac{\sum_{y=2081}^{2098} (DE_i^{(y)} - T_i^{(y)})^2}{18}}$$

$$median\ per\ year\ (21\ DNNs\ ensemble) = med_{DNNs,i}^{(y)} = median\ of\ \{\hat{T}_{m,i}^{(y)}\}$$

$$5\%\ per\ year\ (21\ DNNs\ ensemble) = 5\%_{DNNs,i}^{(y)} = 5\%\ of\ \{\hat{T}_{m,i}^{(y)}\}$$

$$95\%\ per\ year\ (21\ DNNs\ ensemble) = 95\%_{DNNs,i}^{(y)} = 95\%\ of\ \{\hat{T}_{m,i}^{(y)}\}$$

$$5\%\ per\ year\ (21\ CMIP6\ ensemble) = 5\%_{CMIP6,i}^{(y)} = 5\%\ of\ \{T_{m,i}^{(y)}\}$$

$$95\%\ per\ year\ (21\ CMIP6\ ensemble) = 95\%_{CMIP6,i}^{(y)} = 95\%\ of\ \{T_{m,i}^{(y)}\}$$

where:

- $\{\hat{T}_{m,i}^{(y)}\}$  is the set of global temperature values predicted by the 21 DNNs (each pre-trained on one of the  $m$  CMIP6 models and fine-tuned on the taken-out model  $i$ ) for year  $y$
- $\{T_m^{(y)}\}$  is the set of global temperature values simulated by the remaining 21 CMIP6 models when model  $i$  is used as taken-out model

$$Avg\ med_{DNNs,i} = \frac{1}{18} \sum_{y=2081}^{2098} (med_{DNNs,i}^{(y)})$$

$$Avg\ 5\%_{DNNs,i} = \frac{1}{18} \sum_{y=2081}^{2098} (5\%_{DNNs,i}^{(y)})$$

$$Avg\ 95\%_{DNNs,i} = \frac{1}{18} \sum_{y=2081}^{2098} (95\%_{DNNs,i}^{(y)})$$

$$Avg\ 5\%_{CMIP6,i} = \frac{1}{18} \sum_{y=2081}^{2098} (5\%_{CMIP6,i}^{(y)})$$

$$Avg\ 95\%_{CMIP6,i} = \frac{1}{18} \sum_{y=2081}^{2098} (95\%_{CMIP6,i}^{(y)})$$

$$\% \text{ Uncertainty reduction}_i = \frac{(Avg\ 95\%_{CMIP6,i} - Avg\ 5\%_{CMIP6,i}) - (Avg\ 95\%_{DNNs,i} - Avg\ 5\%_{DNNs,i})}{(Avg\ 95\%_{CMIP6,i} - Avg\ 5\%_{CMIP6,i})} * 100$$

$$Avg_i = \frac{1}{18} \sum_{y=2081}^{2098} (T_i^{(y)})$$

$$Accuracy_i = Avg\ med_{DNNs,i} - Avg_i$$

The mean values reported at the bottom of Table S2 are computed as follows:

$$\text{Mean global average error} = \frac{1}{22} \sum_{i=1}^{22} |\text{Global average error}_i|$$

$$\text{Mean global RMSE} = \frac{1}{22} \sum_{i=1}^{22} (\text{Global RMSE}_i)$$

$$\text{Mean accuracy} = \frac{1}{22} \sum_{i=1}^{22} (\text{Accuracy}_i)$$

Some of these values are used to plot Figs. S5 and S6. Indeed, the following quantities are used to plot the red and light blue bars corresponding to each iteration of the leave-one-out cross validation, in which CMIP6 model  $i$  is used removed from the ensemble and used as taken-out model. Specifically,  $\text{Avg } 5\%_{\text{CMIP6},i}$  and  $\text{Avg } 95\%_{\text{CMIP6},i}$  are the average 5% and average 95% of the global temperatures simulated by the remaining CMIP6 models of the ensemble and used to plot the red bar.  $\text{Avg med}_{\text{CMIP6},i}$  is the median of the global temperatures simulated by the remaining CMIP6 models and used to plot the corresponding white line.

$\text{Avg } 5\%_{\text{DNNs},i}$  and  $\text{Avg } 95\%_{\text{DNNs},i}$  are the average 5% and average 95% of the global temperatures predicted by the DNNs (fine-tuned on taken-out model  $i$ ) in each iteration and used to plot the light blue bar.  $\text{Avg med}_{\text{DNNs}}$  is the median of the global temperatures predicted by the DNNs (fine-tuned on taken-out model  $i$ ) in each iteration and used to plot the corresponding white line.

$\text{Avg}_i$  is the average global temperature simulated by the taken-out CMIP6 model  $i$  and used to plot the black and dashed lines.

# Supplementary Text

## Additional results

In the present supplementary section several additional results are described to foster the interpretation of the approach and provide further information.

Fig. S2 reports the predictions generated by the 22 DNNs after their training on the 22 CMIP6 simulations for each scenario. The DNNs are trained on the entire 1850–2098 period (validation year: 2095) to map the annual CO<sub>2</sub> equivalent scalar value to the corresponding global surface temperature field for the same year (Fig. S1A). The DNNs accurately reproduce the models' simulations they are trained on showing less variability as expected, as they are not meant to predict interannual variability but only the response to the forcing. This confirms that the DNNs capture both historical and future temporal patterns during the first training.

To prove that also the spatial information is retrieved by the DNNs during this phase, Fig. S3 shows — for each scenario — the difference of the DNNs ensemble with respect to the CMIP6 ensemble for the year 2095 used as validation during the pre-training phase. Before TL, the models can reproduce the temperature maps without any sign of overfitting even on the part of the data that was reserved for validation.

One of the main contributions of the present work is the generation of global surface air temperature maps instead of just scalar values. This allows taking into account the pattern effect which is critical for climate sensitivity. As shown in Fig. S4, the regional differences of the 21 pre-trained DNNs (which emulate the CMIP6 models that were trained on) (Fig. S4A–C)

As shown in Fig. S4, the 21 pre-trained DNNs (which emulate the CMIP6 models that were trained on — Fig. S4A–C) exhibit regional differences with respect to the taken-out model (MIROC6 in Fig. S4). These differences are then adjusted by fine-tuning the pre-trained DNNs on the taken-out model simulation, treated as “synthetic observation” (MIROC6 in Fig. S4), over the historical period (1850–2022). We note a substantial reduction of the regional differences exhibited by the DNNs, confirming that the pattern effect has been considered (Fig. S4D to F).

The achieved results prove that the proposed TL approach is able to correct both the temporal (Fig. 1) and the regional patterns (Fig. S4) of the models even in the long-term future. To this extent, the years reserved for training (1850–2022) during the leave-one-out cross-validation are critical to allow the DNNs to capture the climate change signals from the taken-out model historical simulations. Movie S1 reveals that those signals appear evident from 2000–2005 and are exploited by the DNNs to produce increasingly accurate and precise projections up to the end of the century.

To give a complete representation of the leave-one-out cross-validation results, together with information about the position of each model's projection within the ensemble range, Fig. S5 is provided. In this figure, the confidence range of the temperatures projected by the CMIP6 models and the DNNs for each taken-out model (as described in the section Metrics of Materials and Methods) are compared. It can be evinced that the proposed approach proves effective in narrowing the temperature uncertainty range (i.e., increasing the precision) for all the taken-out models, even for the taken-out models that belong to the extremes of the 5–95%

range, thus for low and high sensitivity climate models (e.g., CanESM5-CanOE, FGOALS-f3-L across all SSPs). Moreover, a good accuracy (i.e., temperatures projected by the DNNs close to the “synthetic observations”) is obtained as well. However, DNNs fail to accurately reproduce the temperatures projected by some of the taken-out models, and this deserves further investigation.

To further show the capacity of our method to replicate CMIP6 models simulations even without any model family lineage, the leave-one-out cross-validation was also performed by excluding, at each iteration, the taken-out model as well as those models sharing the same atmospheric component it is based on. Specifically, the family membership was first identified based on the atmospheric component of each CMIP6 model reported in Table S1. Afterwards, the leave-one-out cross-validation procedure was performed by taking out the selected model, along with its family members. For instance, when ACCESS-CM2 was taken out, KACE-1-0-G and UKESM1-0-LL were excluded as well. The results remain approximately the same if the family members are excluded (Fig. S6) or not (Fig. S5). This confirms that our proposed TL approach is robust and not biased by specific models that share the same lineage.

Furthermore, the proposed TL approach's ability to effectively reduce the uncertainty of the CMIP6 simulations is proven employing a time reversal test (Fig. S7). In particular, 2023–2098 time period was used as training set and 1850–2022 as test set in the leave-one-out cross-validation procedure. As can be noticed in Fig. S7, when ACCESS-CM2 was taken out, the DNNs were able to successfully reverse time across model cases as the DNNs predictions result less spread out than CMIP6 simulations, even if there are uncertainties in the historical aerosol forcing which make this experiment challenging.

The results just discussed represent a proof of the efficacy of applying TL on observational data to reduce models' uncertainty in projecting future temperatures. In addition, the projections generated by the DNNs ensemble after TL on observational data were compared to the DNNs solely trained on observations (Fig. S8). The latter can accurately replicate historical data but are unable to properly follow the CMIP6 projections as expected, confirming that the TL on observational data is effectively fusing the future climate knowledge deriving from the DNNs pre-trained on the entire 1850–2098 period with the past observed temperatures.

## **Structural and parametric errors**

Two natural questions come to mind after seeing the performance of the DNNs. First, why can the neural network project climate change so well? And, second, isn't the historical data used twice given that some of them are used during the model tuning? Those two questions boil down to the same underlying causes. Earth system models are a simplified representation of the complex physical, chemical and biological processes of the real world. As such, they inherently make assumptions regarding the representation of the processes in terms of the equations and their structure (e.g., the complexity), as well as the values of parameters used in those equations. Some of the available historical data are used to tune the major model parameters (e.g., cloud entrainment rate or microphysical parameters) to match the historical climatology or some modes of climate variability such as El Niño (68, 69). Yet, each CMIP6 model is inherently limited by its structural assumptions and thus cannot optimally use existing data as it can only work within a subspace restricted by its inherent structures. Our DNNs,

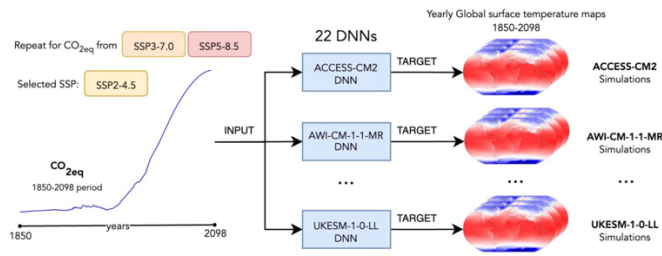
instead, learn how to best leverage both the structurally deficient physics of the climate system and historical data information to improve some of the temperature biases characterizing most of the Earth system models.

One of the major biases of the Earth system models is the cold tongue bias and its extension along the equatorial band typically too cold by about 2°C (70) and present in all the three generations of CMIP models (71). It results to be critical for climate change assessment as it can deteriorate El Niño-Southern Oscillation projections (72). The DNNs ensemble improves the cold tongue bias by predicting higher surface air temperature values than CMIP6 ensemble in the historical period (Fig. 4). Another bias typically present in climate models concerns the Arctic Amplification (47, 73). It has been shown that, during 1979–2021, the Arctic has warmed nearly four times faster and both CMIP5 and CMIP6 models underestimate it (47). The maximum warming is observed in the Eurasian sector of the Arctic Ocean, near Svalbard and Novaya Zemlya, while large continental regions in North America and Western Siberia do not reveal statistically significant trends (47). These patterns are captured and improved by the DNNs ensemble after the inclusion of the observational data and these patterns are exploited to predict historical surface air temperature regional variations (Fig. 4). Furthermore, coupled Earth system models are affected by sea surface temperature (SST) biases in the location and structure of the Gulf Stream (74, 75). In particular, warmer temperatures are simulated in the North Atlantic region centered on the Mid-Atlantic bight where the modeled Gulf Stream separates from the coast further north than observations (76, 77). Besides, a well-known and long-standing issue in ocean modeling concerns the cold bias located to the east of the Grand Banks of Newfoundland (76), where the Gulf Stream ends and the North Atlantic Current begins, even if in some models (78, 79) it is improved by using a higher horizontal resolution (74). Our DNNs improved it as well, generating lower surface air temperatures in the aforementioned region (Fig. 4).

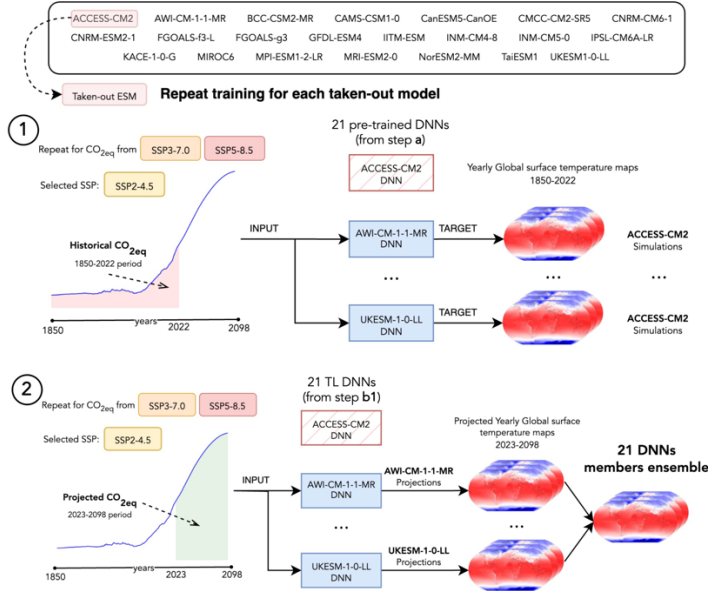
High SSTs in the western Pacific warm pool and low SSTs in the eastern Pacific cold tongue define a zonal contrast in the tropical Pacific atmosphere-ocean state (80) which is a point of contention in future projections (79). Most CMIP models project a higher warming in the equatorial central-eastern Pacific than the western Pacific, which corresponds to a weakening of the SST gradient and often called “El Niño-like” warming pattern (80–85). This must be reconciled with the strengthening of the SST gradient recently observed since the mid-twentieth century (“La Niña-like” warming) (80, 81, 85) and the weakening of the east-west temperature gradient simulated by CMIP6 models (82). Although the observational dataset shows a clear La Niña-like trend (86), determining future response from an unforced natural multidecadal variability or partly from a forced response to anthropogenic climate change is not trivial (84, 85). Yet, the contribution of natural variability to multi-decadal trends appears relatively small in this region, thus the large discrepancy would suggest a systematic bias that models have in response of SST patterns to anthropogenic forcing (84, 86) and that observations are truly outside the model range (81). Furthermore, it has been shown that a physically consistent response to warming could be La Niña-like and that it could have been detectable since the late twentieth century (85), which is aligned with our results (Figs. S9 and S10). Our results reveal that the Transfer Learning approach corrects SST biases that CMIP6 models exhibit in the historical period. Clearly, this does not imply that biases in the future

response (being still unknown) are fully corrected as well, as we have no information about them yet, but this is an encouraging result.

### A Pre-training of individual DNNs on ESMs simulation data



### B Leave-one-out Cross Validation on CMIP6 ESMs simulations



### C Transfer Learning on observations (BEST data)

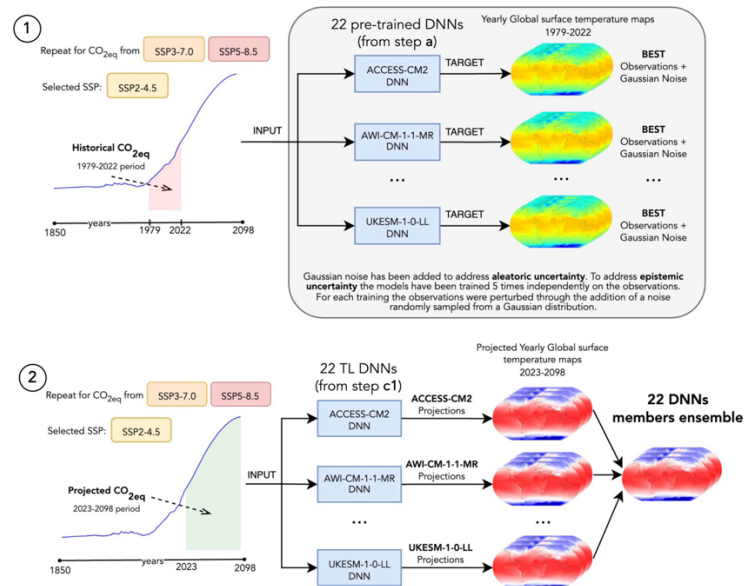
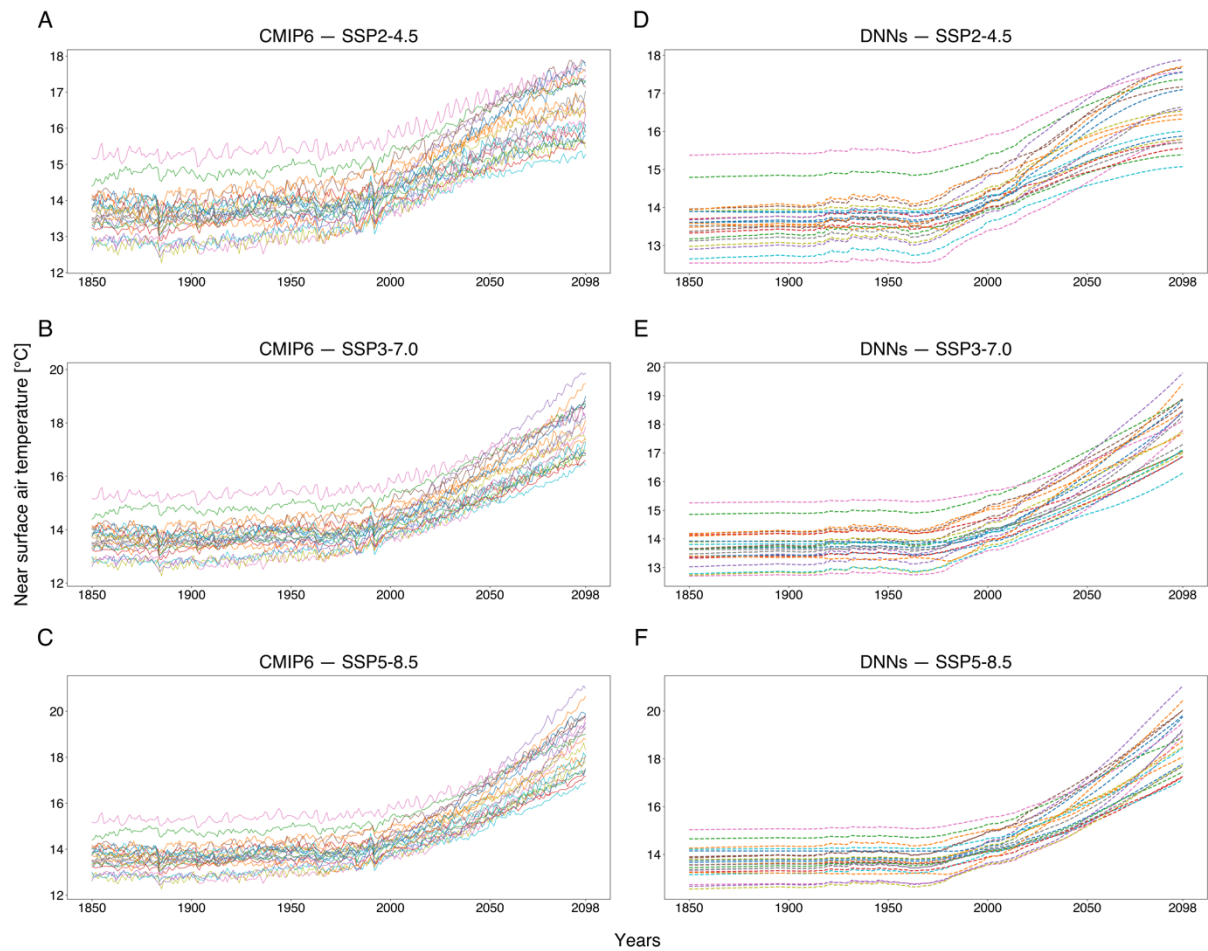
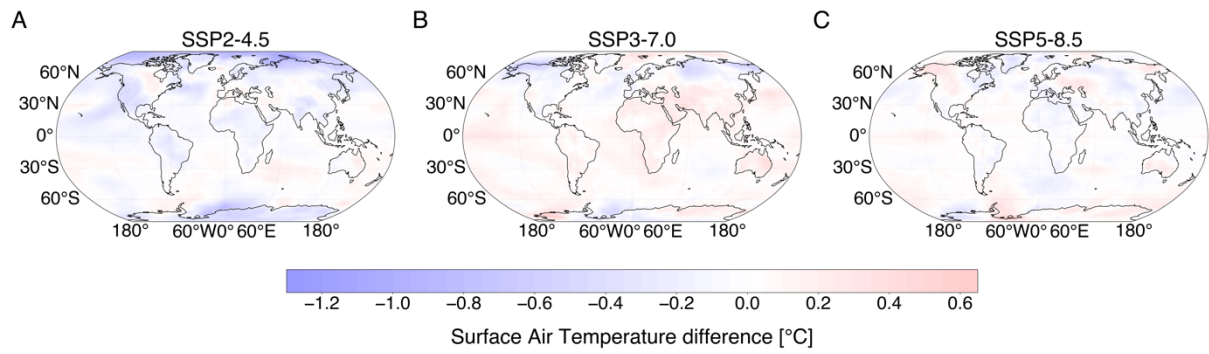


Fig. S1. Leave-One-Out Cross-Validation and Transfer Learning workflows.



**Fig. S2. Pre-training results.** (A to F) Comparison between CMIP6 simulations (A–C, thin dotted lines) and global temperatures generated by DNNs (D–F, thin solid lines). The temperatures are generated after training each DNN on one of the CMIP6 simulations (the one with the same colour) from 1850 to 2095, reserving the year 2095 for validation purposes.



**Fig. S3. Pre-training results on the validation year 2095.** (A to C) Average surface air temperature difference maps generated by the DNNs with respect to the CMIP6 ensemble for each SSP. Each DNN was trained on one of the CMIP6 simulations from 1850 to 2098, reserving the year 2095 for validation purposes. Then, the DNNs predictions as well as CMIP6 simulations were averaged for the year 2095.

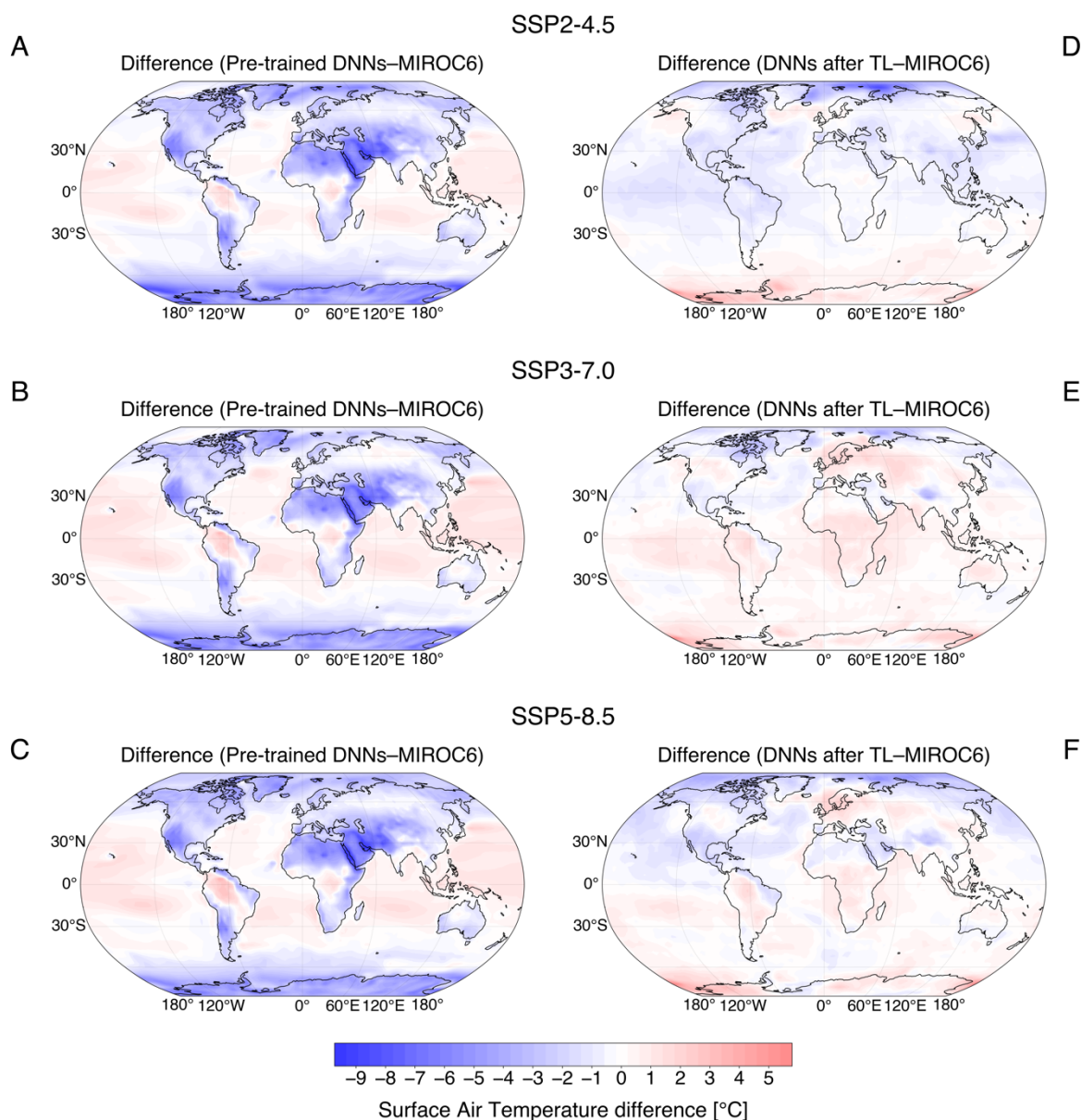


**Fig. S4. Comparison of the results of pre-trained DNNs and DNNs transfer learned on “synthetic observations” (here for MIROC6).** (A to F) Average surface air temperature difference maps generated by the DNNs with respect to the MIROC6 simulation for each SSP in the 2081–2098 period. The maps were generated after pre-training 21 DNNs each on a different CMIP6 simulation (excluding MIROC6) from 1850 to 2098 (A to C) and after transfer learning the pre-trained DNNs on MIROC6 historical simulation data (1850–2022) (D to F). Then, the DNNs ensemble predictions were averaged in 2081–2098.

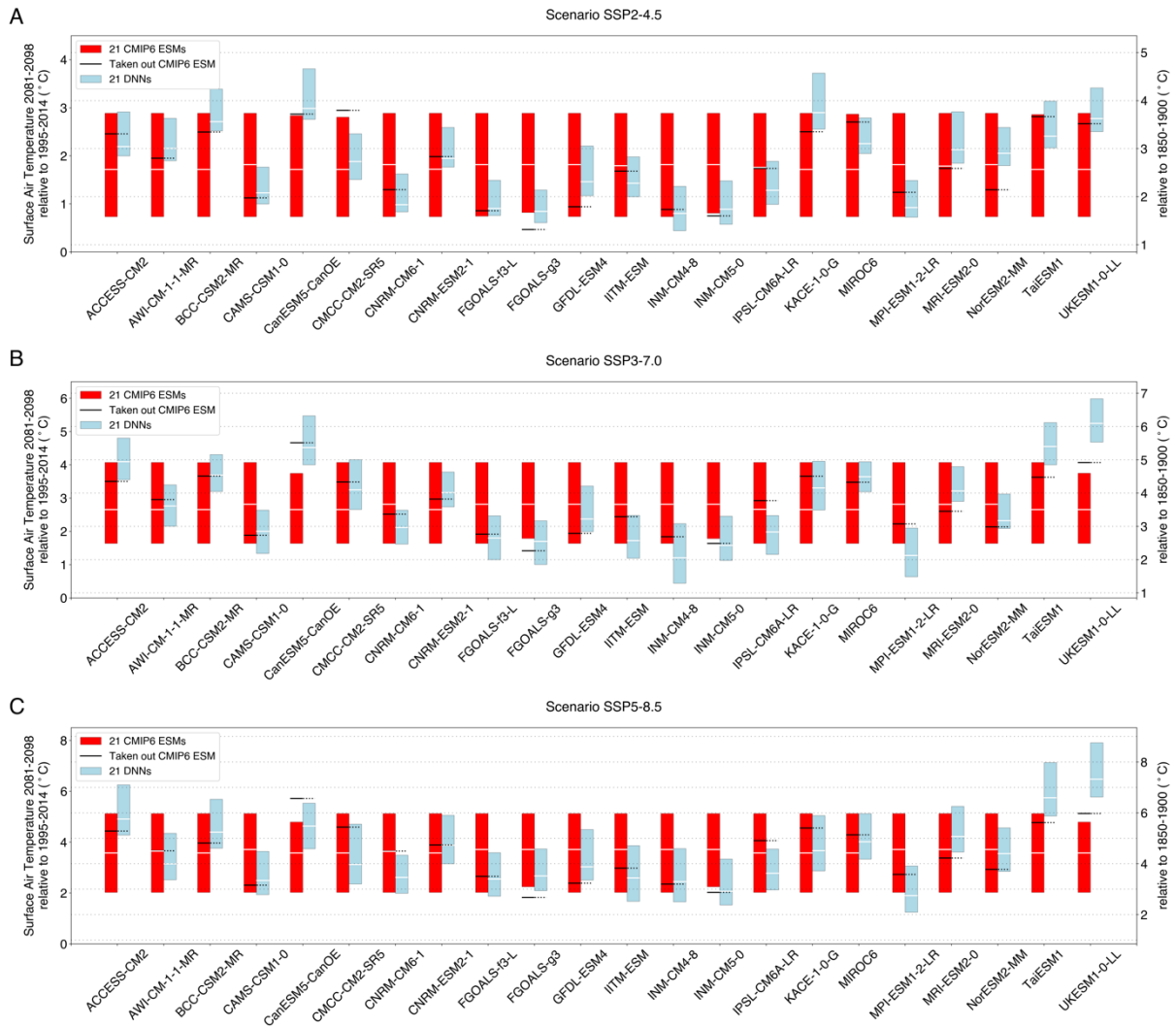


**Fig. S5. Leave-one-out cross-validation results.** (A to C) Accuracy and precision of the DNNs after each iteration of the leave-one-out cross-validation procedure. Each panel shows the global average 5–95% warming ranges for the long-term period (2081–2098) — relative to the average over 1995–2014 (left y axis) and 1850–1900 (right y axis) — simulated by the remaining 21 CMIP6 models (red bar) and predicted by the 21 DNNs ensemble (light blue bar). White lines for each box plot represent the corresponding temporally averaged median values. Black and dashed lines represent the average of the global temperature simulated by the taken-out CMIP6 model. The results are produced for SSPs 2-4.5 (A), 3-7.0 (B) and 5-8.5 (C).

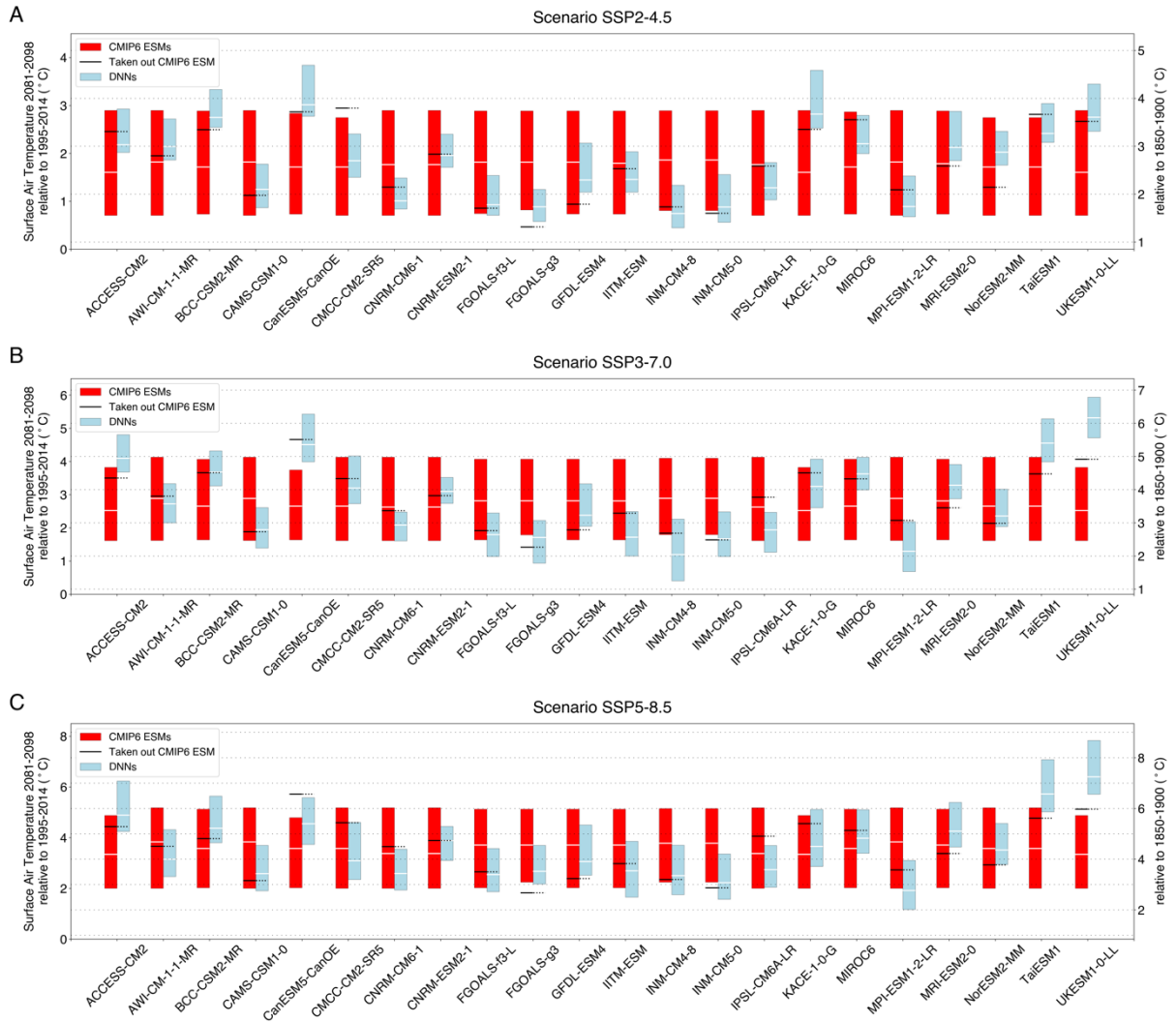


**Fig. S6. Leave-one-out cross-validation results excluding (in turn) the taken-out CMIP6 model and those sharing its atmospheric model. (A to C)** Accuracy and precision of the DNNs after each iteration of the leave-one-out cross-validation procedure. Besides the taken-out CMIP6 model, in each iteration we also excluded those sharing the same atmospheric model (Table S1). Each panel shows the global average 5–95% warming ranges for the long-term period (2081–2098) — relative to the average over 1995–2014 (left y axis) and 1850–1900 (right y axis) — simulated by the remaining CMIP6 models (red bar) and predicted by the DNNs ensemble (light blue bar). White lines for each box plot represent the corresponding temporally averaged median values. Black and dashed lines represent the average of the global temperature simulated by the taken-out CMIP6 model. The results are produced for SSPs 2-4.5 (A), 3-7.0 (B) and 5-8.5 (C).

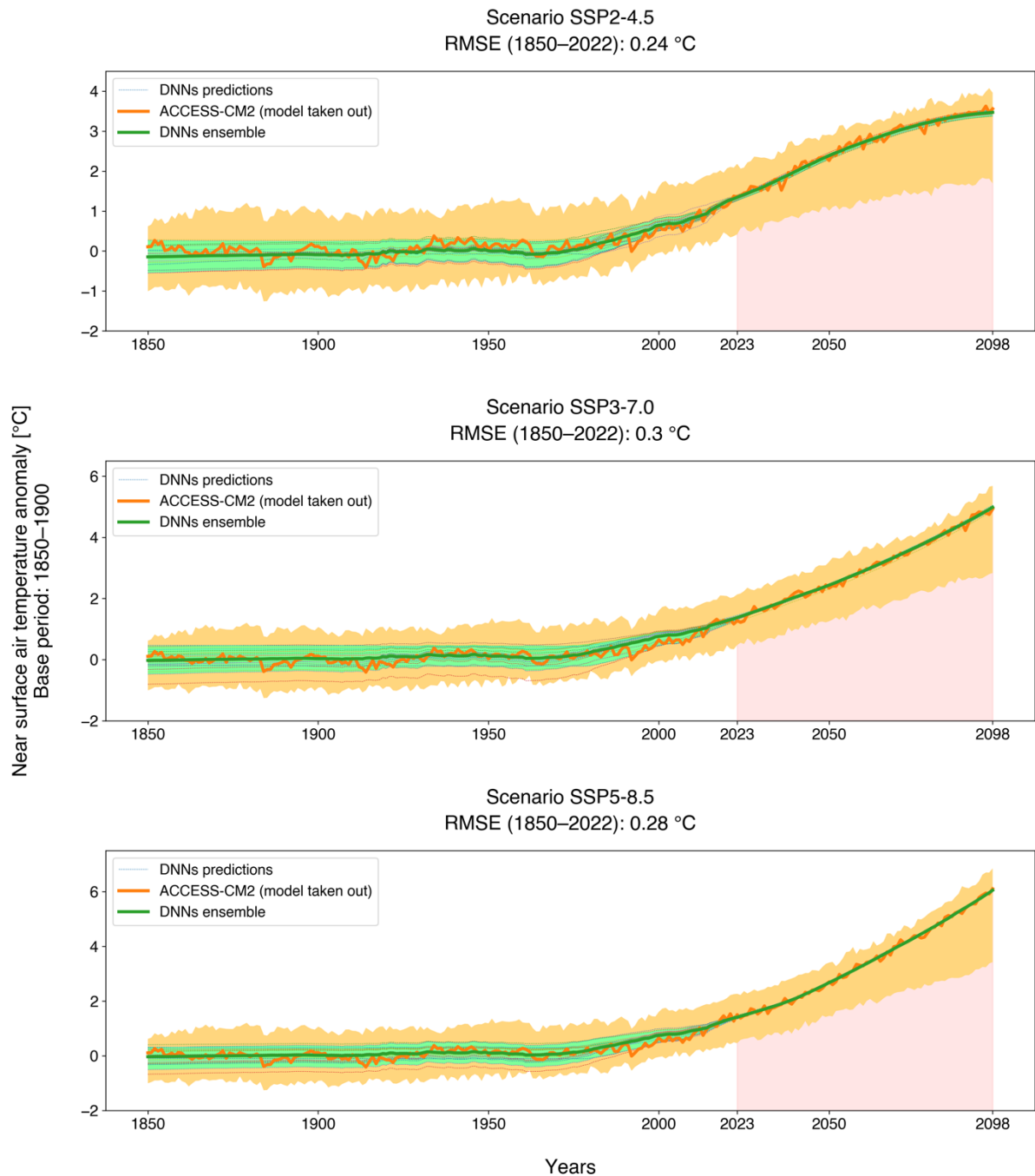


**Fig. S7. Leave-One-Out Cross-Validation (reversing time, here for ACCESS-CM2).** Global average surface air temperature projected by the DNNs (thin dotted lines), corresponding averages across the DNNs (DNNs ensemble, bold green line) for each scenario and ACCESS-CM2 simulation data (orange bold line). The historical temperatures in 1850–2022 are generated after transfer learning each DNN on the ACCESS-CM2 projections (2023–2098). Red shadings show the training set (2023–2098); green shadings show the 5–95% range of the DNNs ensemble; yellow shadings show the 5–95% of the CMIP6 ensemble.

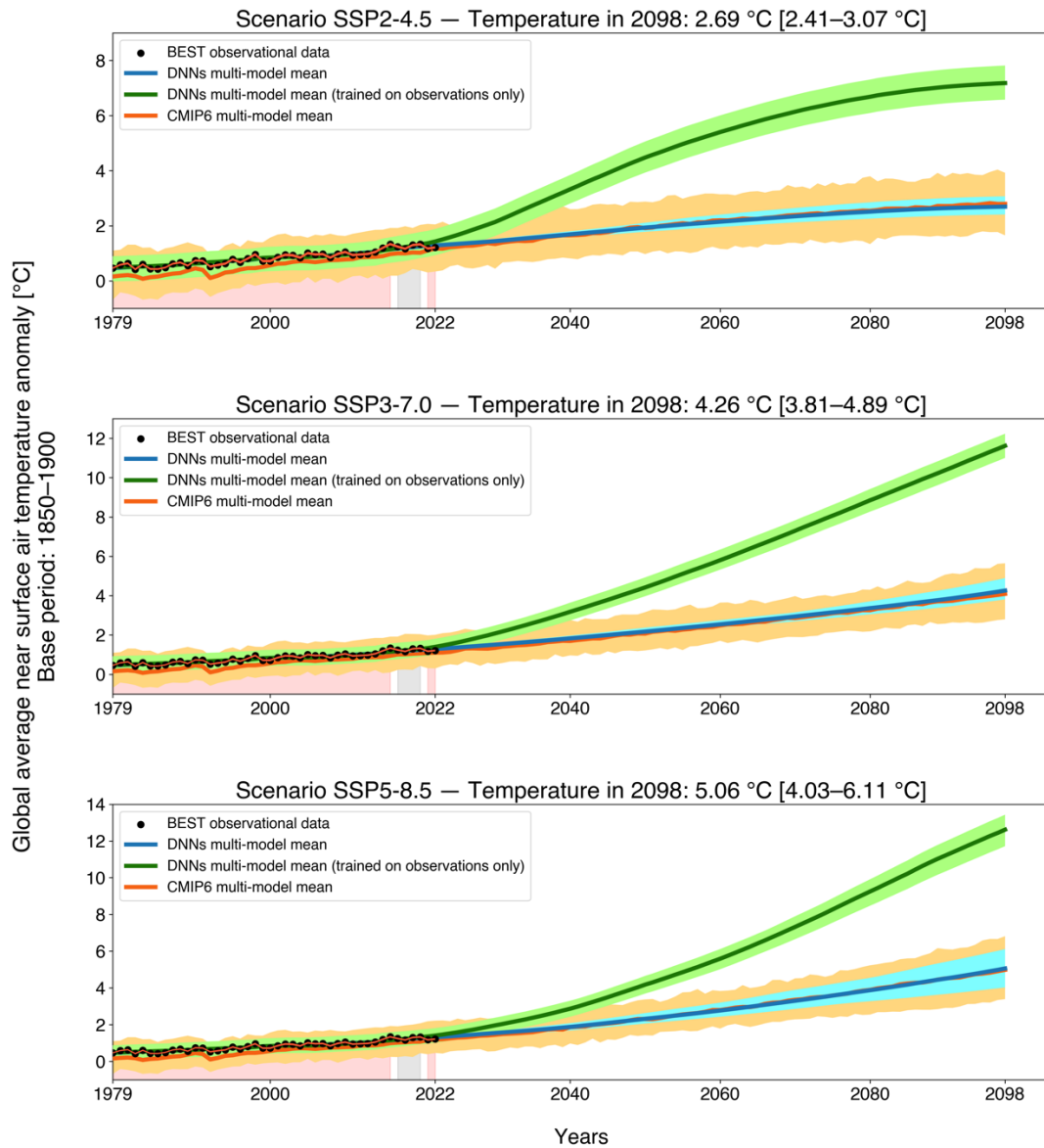


**Fig. S8. Comparison of DNNs trained on observations only (without CMIP6 model pretraining) and DNNs pre-trained on CMIP6 models and then transfer learned on observational data.** DNNs multi-model mean projections of global average surface air temperature for each scenario. The bold blue line refers to the ensemble projections of DNNs transfer learned (training set, red shading: 1979–2016, 2021, 2022; validation set, grey shading: 2017–2020) on BEST-perturbed historical observational data (black dots). The bold green line refers to the ensemble projections of DNNs solely trained on the aforementioned BEST dataset. The 5–95% projections ranges of DNNs transfer learned on observations (light blue shading), DNNs trained on observations only (light green shadings) and CMIP6 unconstrained (orange shading) are also reported. The unconstrained CMIP6 multi-model mean (bold orange line) is shown as well. For each plot, numerical values of 5–95% range for temperature prediction in 2098 (the last projection year) are present in square brackets. The DNNs trained only on observations cannot correctly project the future, unlike our transfer learning approach.

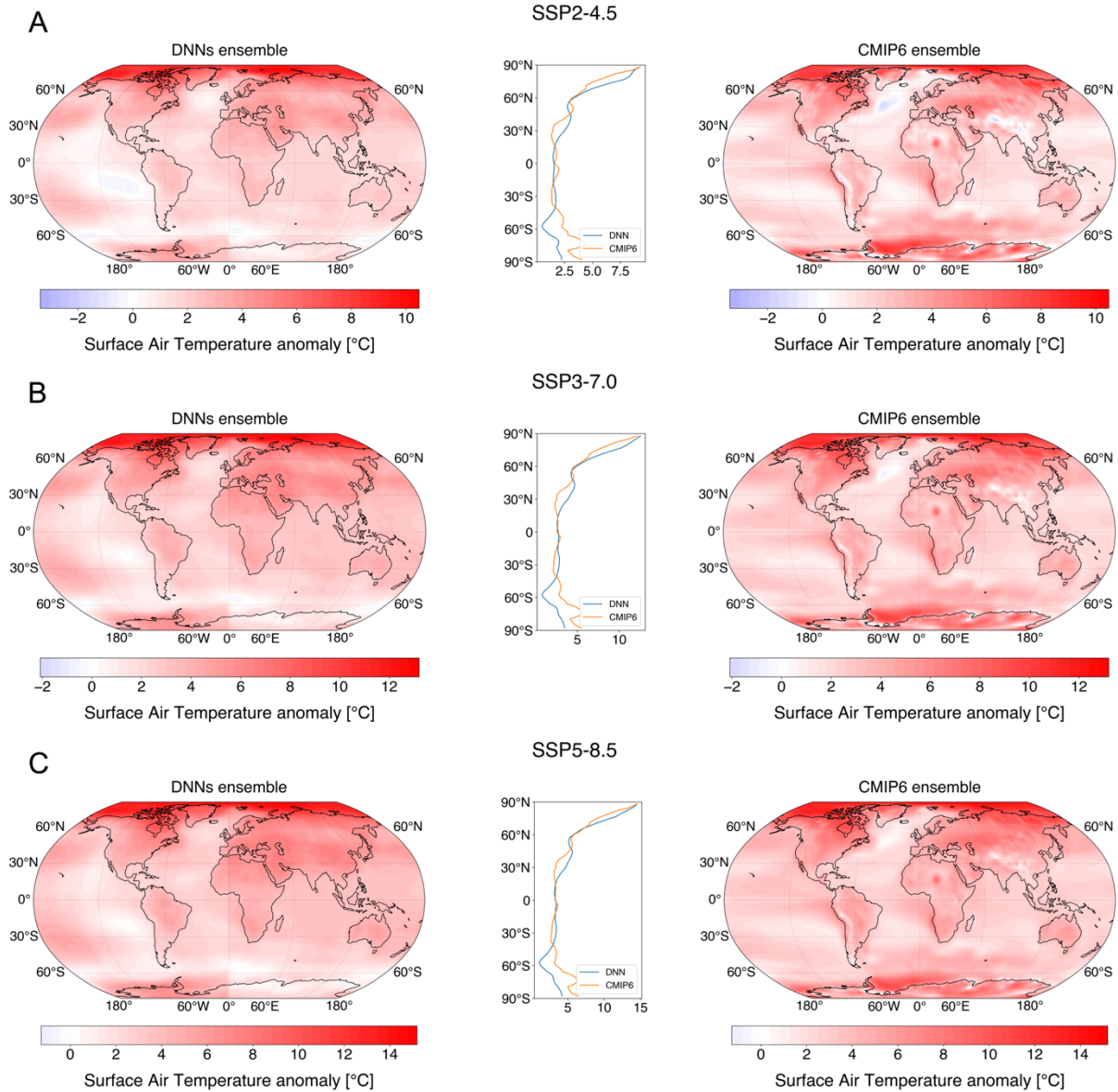


**Fig. S9. Long-term surface air temperature anomaly maps and temperature variation across latitudes.** (A to C) Surface air temperature anomaly maps in 2081–2098 with respect to the 1980–1990 base period. They are computed by averaging in time the temperature maps generated by the DNNs (left) and CMIP6 models (right) for SSP2-4.5 (A), SSP3-7.0 (B) and SSP5-8.5 (C) scenarios. The maps are produced by the DNNs after transfer learning them on observations. The variation of temperatures across latitudes is also reported (center).

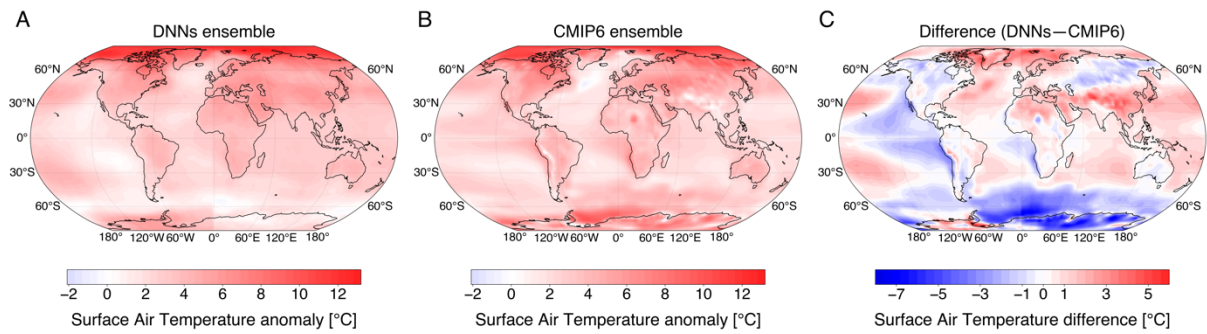


**Fig. S10. Long-term surface air temperature anomaly maps.** (A to C) Surface air temperature anomaly maps in 2081–2098 with respect to the 1980–1990 base period for the SSP3-7.0 scenario. They are computed by averaging in time (between 2081 and 2098) the temperature maps generated by the DNNs (A) and CMIP6 models (B). The difference between DNNs and CMIP6 average maps is also reported (C). The maps are produced by the DNNs after transfer learning them on observations.

<b>Coupled model</b>	<b>Atmospheric model</b>	<b>Reference</b>	<b>Identifier</b>
ACCESS-CM2	MetUM-HadGEM3-GA7.1, 192x144, 85 lv	Bi et al., 2020 (87)	r1ilp1f1
AWI-CM-1-1-MR	ECHAM6.3.04p1, 384x192, T127L95, 95 lv	Semmler et al., 2020 (88)	r1ilp1f1
BCC-CSM2-MR	BCC-AGCM3-MR, 320x160, 46 lv	Wu et al., 2021 (89)	r1ilp1f1
CAMS-CSM-1-0	ECHAM5_CAMS, 320x160, 31 lv	Rong et al., 2019 (90)	r1ilp1f1
CanESM5-CanOE	CanAM5, 128x64, 49 lv	Swart et al., 2019 (91)	r1ilp2f1
CMCC-CM2-SR5	CAM5.3, 288x192, 30 lv	Cherchi et al., 2019 (92)	r1ilp1f1
CNRM-CM6-1	ARPEGE 6.3 256x128, 91 lv, T127 Gr 24572 gb	Voltaire et al., 2019 (93)	r1ilp1f2
CNRM-ESM2-1	ARPEGE 6.3, 720x360, T127 Gr 24572 gb, 91 lv	Séférian et al., 2019 (94)	r1ilp1f2
FGOALS-f3-L	FAMIL2.2, 360x180, 32 lv	He et al., 2019 (95)	r1ilp1f1
FGOALS-g3	GAMIL3, 180x80, hybrid, 26 lv	Pu et al., 2020 (96)	r1ilp1f1
GFDL-ESM4	GFDL-AM4.1, 360x180, 49 lv	Dunne et al., 2020 (97)	r1ilp1f1
IITM-ESM	IITM-GFSv1, 192x94, 64 lv	Raghavan et al., 2021 (98)	r1ilp1f1
INM-CM4-8	INM-AM4-8, 180x120, 21 lv	Volodin et al., 2018 (99)	r1ilp1f1
INM-CM5-0	INM-AM5-0, 180x120, 73 lv	Volodin and Gritsun, 2018 (100)	r1ilp1f1
IPSL-CM6A-LR	LMDZ NPv6, 144x143, N96L79, 79 lv	Boucher et al., 2020 (101)	r1ilp1f1
KACE-1-0-G	MetUM-HadGEM3-GA7.1, 192x144, 85 lv	Lee et al., 2020 (102)	r1ilp1f1
MIROC6	CCSR AGCM, 256x128, T85L81, 81 lv	Tatebe et al., 2019 (103)	r1ilp1f1
MPI-ESM1-2-LR	ECHAM6.3, 192x96, T63L95, 47 lv	Mauritsen et al., 2019 (104)	r1ilp1f1
MRI-ESM2-0	MRI-AGCM3.5, 320x160, TL159L80, 80 lv	Yukimoto et al., 2019 (105)	r1ilp1f1
NorEMS2-MM	CAM-Oslo, 288x192, 32 lv;	Seland et al., 2020 (106)	r1ilp1f1
TaiESM1	TaiAM1, 288x192, 30 lv	Wang et al., 2021 (107)	r1ilp1f1
UKESM1-0-LL	MetUM-HadGEM3-GA7.1, 192x144, 85 lv	Sellar et al., 2019 (108)	r1ilp1f2

**Table S1. CMIP6 Earth system models.** List of CMIP6 Earth system models used in this work and their atmospheric model lineage. Notice that CMCC-CM2-SR5, NorESM2-MM, and

TaiESM1 do not share the same atmospheric model, but are still related. Indeed, they leverage atmospheres based on the Community Atmosphere Model (109) developed at the National Center for Atmospheric Research. Thus, they are considered sharing the same lineage in this work.

Taken-out model	Scenario	Global average error [°C]	Global RMSE [°C]	% uncertainty reduction	Accuracy	Avg 5% [°C]	Avg 95% [°C]
ACCESS-CM2	SSP2-4.5	-0.13	0.14	57.42	-0.26	2.0	2.91
	SSP3-7.0	0.63	0.65	48.58	0.59	3.55	4.8
	SSP5-8.5	0.59	0.6	36.21	0.47	4.27	6.25
AWI-CM-1-1-MR	SSP2-4.5	0.26	0.29	59.02	0.2	1.9	2.78
	SSP3-7.0	-0.23	0.27	48.77	-0.2	2.15	3.4
	SSP5-8.5	-0.41	0.43	41.07	-0.51	2.52	4.34
BCC-CSM2-MR	SSP2-4.5	0.33	0.34	59.54	0.21	2.52	3.39
	SSP3-7.0	0.04	0.11	54.27	0.03	3.2	4.31
	SSP5-8.5	0.56	0.59	37.94	0.43	3.76	5.68
CAM5-CSM1-0	SSP2-4.5	0.19	0.22	64.39	0.11	1.0	1.76
	SSP3-7.0	0.06	0.15	46.25	0.12	1.33	2.64
	SSP5-8.5	0.35	0.37	45.22	0.19	1.93	3.63
CanESM5-CanOE	SSP2-4.5	0.28	0.29	49.98	0.12	2.76	3.81
	SSP3-7.0	-0.05	0.1	30.18	-0.15	4.0	5.47
	SSP5-8.5	-1.15	1.17	35.18	-1.09	3.74	5.53
CMCC-CM2-SR5	SSP2-4.5	-1.05	1.06	54.15	-1.06	1.51	2.46
	SSP3-7.0	-0.21	0.26	38.6	-0.24	2.66	4.15
	SSP5-8.5	-1.33	1.34	24.14	-1.47	2.35	4.71
CNRM-CM6-1	SSP2-4.5	-0.19	0.24	63.28	-0.31	0.83	1.62
	SSP3-7.0	-0.42	0.43	57.98	-0.4	1.62	2.64
	SSP5-8.5	-0.92	0.94	51.54	-1.04	1.98	3.49
CNRM-ESM2-1	SSP2-4.5	0.11	0.17	61.74	-0.04	1.77	2.59
	SSP3-7.0	0.21	0.24	56.98	0.19	2.74	3.78
	SSP5-8.5	0.05	0.09	38.65	-0.01	3.15	5.05

Taken-out model	Scenario	Global average error [°C]	Global RMSE [°C]	% uncertainty reduction	Accuracy	Avg 5% [°C]	Avg 95% [°C]
FGOALS-f3-L	SSP2-4.5	0.17	0.2	65.83	0.05	0.76	1.49
	SSP3-7.0	-0.11	0.17	45.67	-0.11	1.15	2.47
	SSP5-8.5	-0.07	0.14	44.85	-0.1	1.87	3.58
FGOALS-g3	SSP2-4.5	0.42	0.43	67.03	0.38	0.61	1.29
	SSP3-7.0	0.2	0.21	42.48	0.28	1.0	2.32
	SSP5-8.5	1.0	1.0	42.81	0.85	2.09	3.73
GFDL-ESM4	SSP2-4.5	0.61	0.62	51.91	0.52	1.17	2.2
	SSP3-7.0	0.58	0.6	43.75	0.43	1.99	3.36
	SSP5-8.5	0.91	0.92	35.74	0.65	2.5	4.5
IITM-ESM	SSP2-4.5	-0.16	0.19	61.51	-0.25	1.15	1.98
	SSP3-7.0	-0.62	0.62	47.14	-0.72	1.19	2.48
	SSP5-8.5	-0.29	0.31	29.34	-0.38	1.67	3.86
INM-CM4-8	SSP2-4.5	-0.06	0.07	57.08	-0.08	0.44	1.36
	SSP3-7.0	-0.6	0.6	26.26	-0.63	0.44	2.23
	SSP5-8.5	0.16	0.17	32.59	0.1	1.65	3.74
INM-CM5-0	SSP2-4.5	0.19	0.2	56.54	0.14	0.57	1.48
	SSP3-7.0	0.05	0.12	41.77	-0.06	1.13	2.46
	SSP5-8.5	0.2	0.21	37.13	0.04	1.53	3.33
IPSL-CM6A-LR	SSP2-4.5	-0.39	0.42	58.37	-0.46	0.99	1.89
	SSP3-7.0	-0.98	1.01	51.94	-0.94	1.3	2.47
	SSP5-8.5	-1.19	1.2	48.19	-1.29	2.12	3.73
KACE-1-0-G	SSP2-4.5	0.48	0.49	45.78	0.4	2.55	3.72
	SSP3-7.0	-0.45	0.45	39.73	-0.35	2.64	4.11
	SSP5-8.5	-0.76	0.77	29.81	-0.89	2.87	5.04

Taken-out model	Scenario	Global average error [°C]	Global RMSE [°C]	% uncertainty reduction	Accuracy	Avg 5% [°C]	Avg 95% [°C]
MIROC6	SSP2-4.5	-0.41	0.43	65.22	-0.45	2.05	2.79
	SSP3-7.0	0.18	0.25	62.82	0.16	3.19	4.09
	SSP5-8.5	-0.17	0.23	42.29	-0.28	3.33	5.12
MPI-ESM1-2-LR	SSP2-4.5	-0.23	0.25	64.43	-0.32	0.72	1.49
	SSP3-7.0	-0.92	0.93	39.92	-0.95	0.64	2.1
	SSP5-8.5	-0.71	0.72	41.42	-0.83	1.25	3.06
MRI-ESM2-0	SSP2-4.5	0.5	0.51	50.23	0.39	1.84	2.92
	SSP3-7.0	0.69	0.71	57.15	0.61	2.9	3.95
	SSP5-8.5	0.91	0.95	42.01	0.85	3.61	5.41
NorESM2-MM	SSP2-4.5	0.82	0.83	63.19	0.76	1.8	2.59
	SSP3-7.0	0.36	0.41	57.34	0.18	2.08	3.12
	SSP5-8.5	0.64	0.67	44.59	0.62	2.84	4.56
TaiESM1	SSP2-4.5	-0.24	0.26	54.14	-0.41	2.16	3.14
	SSP3-7.0	0.93	0.94	47.77	0.92	4.0	5.27
	SSP5-8.5	1.06	1.1	32.28	0.98	5.03	7.13
UKESM1-0-LL	SSP2-4.5	0.21	0.23	57.83	0.11	2.5	3.41
	SSP3-7.0	1.23	1.24	38.24	1.18	4.68	5.99
	SSP5-8.5	1.42	1.44	22.79	1.35	5.77	7.91
Mean values	SSP2-4.5	0.34	0.36	-	0.32	-	-
	SSP3-7.0	0.44	0.48	-	0.43	-	-
	SSP5-8.5	0.68	0.70	-	0.66	-	-

**Table S2. Leave-one-out cross-validation results.** Global average error, global RMSE, percentage of uncertainty reduction, accuracy, average 5% and 95% with respect to the average of temperatures (predicted by the DNNs) in 2081–2098 computed in the leave-one-model-out cross validation approach for each of the 22 models and the three SSPs (see Metrics section of

Materials and Methods). Each model is the taken-out model considered as synthetic ground truth.

	SSP2-4.5 (°C)	SSP3-7.0 (°C)	SSP5-8.5 (°C)
Ribes et al. (42) (2081–2098)	1.22–2.44 (48%)	2.07–3.47 (37%)	2.4–4.53 (20%)
Liang et al. (43)	1.33–2.72 (55%)	2.28–3.85 (44%)	2.6–4.86 (24%)
Tokarska et al. (41)	1.04–2.56 (59%)	1.75–3.63 (53%)	2.09–4.75 (36%)
IPCC WGI AR6 (46)	1.2–2.6 (55%)	2.0–3.7 (48%)	2.4–4.8 (29%)
CMIP6 ensemble	0.74–2.88 (71%)	1.64–4.05 (63%)	2.03–5.1 (44%)
This work (2081–2098)	1.44–2.07	2.51–3.39	2.74–4.45

**Table S3. Spread of global surface air temperature changes for the long-term period (2081–2100).** Global 5–95% warming ranges for the long-term period (2081–2100) relative to the average over 1995–2014 for SSPs 2-4.5, 3-7.0 and 5-8.5. We also report the percentage reduction in the spread of our approach with respect to each other 5–95% range for the same scenario. Notice that the 5–95% ranges for Ribes et al. and this work are computed in the 2081–2098 time period. The remaining ones are computed in the 2081–2100 time period.

	Time period	SSP2-4.5 (°C)	SSP3-7.0 (°C)	SSP5-8.5 (°C)
IPCC WGI AR6 (46)	2021–2040	0.4–0.9 (70%)	0.4–0.9 (64%)	0.5–1.0 (50%)
	2041–2060	0.8–1.6 (58%)	0.9–1.7 (59%)	1.1–2.1 (42%)
This work	2021–2040	0.48–0.63	0.54–0.72	0.53–0.78
	2041–2060	0.87–1.21	1.14–1.47	1.16–1.74

**Table S4. Spread of global surface air temperature changes for the near-term (2021–2040) and the mid-term (2041–2060) period.** Global 5–95% warming ranges for the near-term (2021–2040) and the mid-term (2041–2060) period relative to the average over 1995–2014 for SSP2-4.5, 3-7.0 and 5-8.5 scenarios. We also report the percentage reduction in the spread of our approach with respect to each other 5–95% range for the same scenario.

	Threshold	SSP2-4.5 (°C)	SSP3-7.0 (°C)	SSP5-8.5 (°C)
Diffenbaugh and Barnes (51)	1.5°C	2033 (2028–2039)	2035 (2030–2040)	-
	2°C	2049 (2043–2055)	2050 (2043–2058)	-
This work	1.5°C	2033 (2029–2036)	2030 (2027–2033)	2029 (2026–2034)
	2°C	2054 (2047–2063)	2045 (2041–2049)	2043 (2038–2049)

**Table S5. Time to 1.5°C and 2°C thresholds.** Remaining times to reach 1.5°C and 2°C thresholds with respect to the 1850–1900 time period according to SSP2-4.5, 3-7.0 and 5-8.5 scenarios.